Entrainment versus Dilution in Tropical Deep Convection

WALTER M. HANNAH

Lawrence Livermore National Laboratory, Livermore, California

ABSTRACT

The distinction between entrainment and dilution is investigated with cloud-resolving simulations of deep convection in a tropical environment. A method for estimating the rate of dilution by entrainment and detrainment is presented and calculated for a series of bubble simulations with a range of initial radii. Entrainment generally corresponds to dilution of convection, but the two quantities are not well correlated. Core dilution by entrainment is significantly reduced by the presence of a shell of moist air around the core. Dilution by entrainment also increases with increasing updraft velocity but only for sufficiently strong updrafts. Entrainment contributes significantly to the total net dilution, but detrainment and the various source/sink terms play large roles depending on the variable in question. Detrainment has a concentrating effect on average that balances out the dilution by entrainment. The experiments are also used to examine whether entrainment or dilution scale with cloud radius. The results support a weak negative relationship for dilution but not for entrainment. The sensitivity to resolution is briefly discussed. A toy Lagrangian thermal model is used to demonstrate the importance of the cloud shell as a thermodynamic buffer to reduce the dilution of the core by entrainment. The results suggest that explicit cloud heterogeneity may be a useful consideration for future convective parameterization development.

1. Introduction

Entrainment has long been recognized as a key process in moist convection (Simpson 1971; Emanuel 1994), which limits the height and intensity through the addition of dry ambient air into a moist updraft (Derbyshire et al. 2004; Del Genio 2012). However, accurately representing the effects of entrainment in models of moist convection remains difficult. Part of the problem is that it is unclear how to constrain the rate of mass entrainment, as well as how it is affected by the properties of the convecting element and the ambient environment. There is strong evidence that cumulus convection does not form without dilution (Romps and Kuang 2010), and thus entrainment has a lower limit larger than zero that models should reproduce. On the other hand, when a minimum entrainment rate is enforced in parameterized convection, there are often undesirable effects, such as unrealistic moisture sensitivity and a degradation of a model's mean state (Kim et al. 2011).

Several issues have been identified in global models associated with the treatment of entrainment in convective parameterizations. One such problem is that too many clouds penetrate the upper troposphere, while too few clouds are found at lower levels (Chepfer et al. 2008). Zhang et al. (2010) showed that increasing the entrainment rate of deep convection could reduce the frequency of the highest clouds, but the overall frequency of precipitation remained too high. Other studies have shown that setting a minimum entrainment threshold can improve the representation of the Madden–Julian oscillation (Maloney and Hartmann 2001; Hannah and Maloney 2011), but other work suggests that this method gets the right answer for the wrong reason by compensating for weak cloud-radiative feedbacks with erroneous cloud-moisture feedbacks (Hannah and Maloney 2014).

Advances in computing power have allowed detailed examinations of small-scale turbulent circulations and interfacial mixing of individual clouds with models run at very fine resolution (Klaassen and Clark 1985; Grabowski and Clark 1993). These studies find that mixing and entrainment occur at the leading edge and wake of a buoyant thermal associated with a toroidal circulation (Zhao and Austin 2005; Sherwood et al. 2013; Romps and Charn 2015), which agrees with laboratory and observational studies (Woodward 1959; Scorer 1957; Johari 1992; Jonas 1990; Stith 1992;

Corresponding author: Walter Hannah, walter@hannahlab.org

Damiani et al. 2006). The shell is thought to be mainly driven by evaporative cooling that results from lateral mixing rather than mechanical forcing (Jonas 1990; Heus and Jonker 2008), although this conclusion may be sensitive to how the shell is defined, specifically whether the shell is restricted to negatively buoyant or subsiding air.

Many studies of entrainment have relied on simplifying assumptions such as negligible detrainment. A steady-state mass budget of a cloud, ignoring changes in cloud area, can be expressed as

$$\frac{\partial M}{\partial z} = e - d, \tag{1}$$

where M is the vertical cloud mass flux and e and d are the total mass entrainment and detrainment rates, respectively. Previous laboratory and observational studies have often relied on budget equations of mass or thermodynamic tracers to indirectly estimate entrainment. However, some of these approaches assume negligible detrainment to simplify the problem (Sloss 1967; McCarthy 1974; Lu et al. 2012), which has been shown to be a very poor assumption (Siebesma and Cuijpers 1995; Romps 2010; Dawe and Austin 2011a; Yeo and Romps 2013). Other studies using thermodynamic tracer budgets to estimate entrainment and detrainment often assume that entrained air is identical to the far-field, cloud-free environment (de Rooy and Siebesma 2010). This approach ignores the shell of saturated air that surrounds the cloud core and also leads to an underestimate of entrainment (Romps 2010; Dawe and Austin 2011b).

Another assumption used to constrain entrainment in some convective parameterizations is that entrainment is inversely proportional to cloud width or radius (Simpson 1971; de Rooy et al. 2013; Arakawa and Schubert 1974; Kain and Fritsch 1990; Zhang and McFarlane 1995). A related simplification is to assume cloud radius is related to the boundary layer depth, which can be used to constrain entrainment (Tokioka et al. 1988). This relationship is rooted in dimensional analysis, similarity theory, and early studies of mixing in jets and buoyant plumes, which include an underlying assumption that turbulent mixing is proportional to the velocity of a convecting fluid (Kuethe 1935; Morton et al. 1956; Turner 1963; Woodward 1959). While laboratory tank experiments have found some support for this assumption (Saunders 1962; Scorer 1957), it remains unclear whether it is valid for accurately parameterizing moist convection. Alternatively, some have related entrainment directly to vertical velocity, which may be a more valid approach (Grant and Brown 1999; Neggers et al. 2002; Chikira and Sugiyama 2010).

Entrainment is often ambiguously described as a mixing process, so it is useful to settle on a more specific definition. Romps (2010) provides a general definition for entrainment as the transition of a volume of air from nonactive to active. Similarly, detrainment is defined as the reverse. This definition offers a flexible concept in the study of fluid dynamics that can be applied to a range of phenomena. For moist convection, active air can mean any volume of saturated air (i.e., cloud), or any volume of saturated air that is moving upward due to buoyant acceleration (i.e., updraft core).

This definition of entrainment allows it to be measured directly. Two methods of directly measuring entrainment in cloud-resolving models were recently developed that allow detailed examination of the processes involved. The method of Romps (2010) uses temporal interpolation to determine when the volume of a model grid cell becomes active, whereas the method of Dawe and Austin (2011a) uses spatial interpolation to identify the cloud boundary within grid cells and estimate fluxes across that boundary. Both give similar results over a sufficient time period, but the latter method allows entrainment to be estimated on short intervals.

Entrainment is often discussed in a way that implies it is synonymous with dilution. Most convective parameterizations are formulated such that this is always the case, but it is unclear whether this is true in the real atmosphere. In light of the issues surrounding entrainment, perhaps instead of asking questions about entrainment rates, we should be asking questions about *dilution rates*. This requires us to make a clear distinction between the two concepts, but luckily, the direct measurement technique is an ideal tool for investigating this.

The purpose of this study is to investigate whether entrainment can be thought of as synonymous to dilution with respect to deep convection in the tropics. Idealized simulations of individual deep convective clouds from the release of a warm humid bubble are used to approach this problem. This allows convection to be investigated systematically, which is difficult to do in simulations of a diverse, interacting cloud population. We will begin by developing a method for estimating dilution rates in section 2 and a description of the experiments in section 3. The simulated clouds are examined in section 4, followed by an analysis of entrainment and dilution rates in section 5 and a brief discussion of resolution sensitivity in section 6. The results of section 5 inspired a toy thermal model with an explicit cloud shell that is discussed in section 7. Conclusions and discussion of the results are presented in section 8.

2. Dilution

To quantify dilution in the context of moist convection, we must first decide how it is defined. Dilution of a given tracer is defined here as a proportional rate of change of the mass-weighted average tracer concentration over a volume of interest. Using a proportional rate of change allows the dilution to reflect the properties of the volume being diluted, in addition to the intensity of the process responsible for the dilution (i.e., entrainment). Following Romps (2010), for a generic tracer ϕ, the three continuity equations are

$$\frac{\partial}{\partial t}\rho + \nabla \cdot (\rho\mathbf{u}) = 0, \tag{2}$$

$$\frac{\partial}{\partial t}(A\rho) + \nabla \cdot (A\rho\mathbf{u}) = e - d, \tag{3}$$

$$\frac{\partial}{\partial t}(\phi\rho) + \nabla \cdot (\phi\rho\mathbf{u}) = S_\phi, \tag{4}$$

where A is the activity operator used to define the cloud or core volume (A is either 1 or 0 depending on whether air is inside or outside the volume of interest, respectively); e and d are the rate of mass entrainment and detrainment, respectively; ρ is the density; $\mathbf{u}$ is the three-dimensional wind vector; and S_ϕ is all the sources and sinks of ϕ.

Using (2), we can rewrite (4) and multiply by A to get

$$A\rho\frac{\partial}{\partial t}\phi + A\rho\mathbf{u} \cdot \nabla\phi = AS_\phi. \tag{5}$$

Using (3), we can pull A, ρ, and $\mathbf{u}$ inside the derivatives:

$$\frac{\partial}{\partial t}(\phi\rho A) + \nabla \cdot (\phi\rho\mathbf{u}A) = e\phi - d\phi + AS_\phi. \tag{6}$$

By assuming that the domain is doubly periodic, or that the horizontal wind goes to zero at the boundaries, we can sum horizontally to get

$$\frac{\partial}{\partial t}\langle\rho A\rangle + \frac{\partial}{\partial z}\langle\rho wA\rangle = \langle e\rangle - \langle d\rangle, \tag{7}$$

$$\frac{\partial}{\partial t}\langle\phi\rho A\rangle + \frac{\partial}{\partial z}\langle\phi\rho wA\rangle = \langle e\phi\rangle - \langle d\phi\rangle + \langle AS_\phi\rangle. \tag{8}$$

A few definitions will simplify the equations going forward:

$$\phi_e = \frac{\langle e\phi\rangle}{\langle e\rangle}, \tag{9}$$

$$\phi_d = \frac{\langle d\phi\rangle}{\langle d\rangle}, \tag{10}$$

$$\phi_c = \frac{\langle\phi\rho A\rangle}{\langle\rho A\rangle} \approx \frac{\langle\phi\rho wA\rangle}{\langle\rho wA\rangle}, \tag{11}$$

$$w_c = \frac{\langle\rho wA\rangle}{\langle\rho A\rangle}. \tag{12}$$

These expressions are simply mass-weighted, and mass-flux-weighted, average quantities. The approximation in (11) is used for notational simplicity, which introduces small errors that only affect the vertical advective tendency when considering a volume with an appreciable mix of upward and downward mass fluxes. The correct formulation is used when calculating the vertical advection term. Next, we will multiply (7) by ϕ_c, subtract from (8), and use (9)–(11) to simplify to get

$$\langle\rho A\rangle\frac{\partial\phi_c}{\partial t} + \langle\rho wA\rangle\frac{\partial\phi_c}{\partial z} = \langle e\rangle(\phi_e - \phi_c)$$
$$- \langle d\rangle(\phi_d - \phi_c) + \langle AS_\phi\rangle. \tag{13}$$

To make the tendencies of ϕ relevant for dilution, we need to divide by the mass-weighted sum of ϕ across the cloud. However, if we use the absolute value of ϕ, then the state of total dilution will be when $\phi = 0$, which does not make physical sense, especially for quantities that will never be absolute zero in the atmosphere, such as moist static energy. A more sensible state of full dilution would be when the cloud volume is indistinguishable from the cloud-free environment. Thus, we can define ϕ' as the deviation from the horizontal average and divide (13) by $\langle\phi'\rho A\rangle$, using (11) and (12) to obtain an expression that approximately describes the proportional change of the mass-weighted average of ϕ in the cloud or core volume depending on how A is defined:

$$\frac{1}{\phi_c'}\frac{\partial\phi_c}{\partial t} + \frac{w_c}{\phi_c'}\frac{\partial\phi_c}{\partial z} = -\frac{\langle e\rangle(\phi_c - \phi_e)}{\langle\phi'\rho A\rangle} + \frac{\langle d\rangle(\phi_c - \phi_d)}{\langle\phi'\rho A\rangle}$$
$$+ \frac{\langle AS_\phi\rangle}{\langle\phi'\rho A\rangle}. \tag{14}$$

The expression in (14) describes proportional tendencies and thus allows us to quantify dilution based on the definition given above. Notice that the terms in (14) have units of per second, so values of each term can be thought of as a *dilution time scale*, similar to an e-folding time scale of an exponential decay equation. Also note that "dilution" corresponds to negative values of the terms in (14), which indicate a tendency of the tracer anomaly toward zero (i.e., state of total dilution). This interpretation of negative proportional tendency values holds for tracers that typically exhibit negative anomalies in active convection, such as the liquid static energy h_L, because of the ϕ in the denominator of right-hand-side terms in (14).

The right-hand side of (14) has components of dilution due to entrainment, detrainment, and any sources/sinks of ϕ. We can understand some intrinsic properties of the

dilution components by considering some limiting cases. For instance, if $\langle e \rangle \approx 0$, then dilution by entrainment will effectively be zero, but if the entrainment is large and $\phi_c \approx \phi_e$, then the dilution by entrainment will also be zero. As for the dilution by detrainment, we can generally expect ϕ_c to have a larger anomaly magnitude than ϕ_d so that detrainment will act to enhance ϕ_c (i.e., concentration). Similarly, if the magnitude of ϕ_e is greater than that of ϕ_c, the cloud will experience concentration of ϕ by entrainment (i.e., negative dilution). Also, if $\phi_c \approx \phi_d$, then the loss of core mass does not affect the average core properties, and dilution by detrainment will be negligible.

3. Methodology

a. The cloud-resolving model

The model used here is the System for Atmospheric Modeling (SAM), version 6.9.5, which solves the anelastic system of momentum equations (Khairoutdinov and Randall 2003). Thermodynamic energy is prognosed with the liquid and ice water static energy,

$$h_L = c_p T + gz - L_c q_l - L_f q_i,$$

where T is absolute temperature, z is height, q_l is liquid condensate, and q_i is ice condensate. This quantity is conserved for all adiabatic processes and water phase transitions but not gravitational sedimentation or radiative heating. The distribution of water is described by two prognostic variables for precipitating (rain, snow, and graupel) and nonprecipitating (vapor, cloud water, and cloud ice) water mixing ratios. The use of these composite prognostic water variables was justified on the basis of computational efficiency (Khairoutdinov and Randall 2006). Sub-grid-scale turbulent fluxes are parameterized with a Smagorinsky-type closure. All simulations presented here are configured with periodic lateral boundary conditions and Newtonian damping in the top three layers to reduce gravity wave reflection. The model domain is set to 25.6 km with 100-m grid spacing in all directions.

Many studies have argued that grid spacing of 100 m or smaller is needed to fully resolve the inertial subrange where turbulent entrainment processes occur (Bryan et al. 2003). The available resources for this study did not permit simulations at finer grid spacing, but experiments were conducted with a coarser 200-m grid for a limited test of how the results might be sensitive to resolution that are discussed in section 6.

b. Experiment setup

To produce tropical deep convection, the model is initialized with a generic tropical sounding calculated from averaging 25 years of ECMWF interim reanalysis (ERA-Interim, hereafter ERAI; Dee et al. 2011) over the equatorial belt from 10°S to 10°N and the period 1990–2014. ERAI data are on a 1° × 1° grid with 19 vertical levels from 1000 to 70 hPa.

To initiate deep convection, a warm humid bubble is added to the initial condition at the center of the domain similar to Yeo and Romps (2013) and Langhans et al. (2015). The bubble perturbations are initialized with a temperature anomaly of 1 K and specific humidity anomaly of 2 g kg^{-1}. These values are realized at the center of the bubble and decrease toward the edge according to a Gaussian distribution to reduce the dispersive effect of gravity waves on the initial temperature perturbation. The center of the bubble is set at an altitude of 500 m with a vertical radius of 1500 m, so the top of the bubble reaches to 2 km, and a portion of the bubble is underground. A small white noise perturbation is also added to the temperature field to foster a turbulent boundary layer, although there is insufficient time to develop a realistic spectrum of turbulent motions in the boundary layer. The model is integrated for 60 min with data written every 30 s to capture the full life cycle of the resulting convection. The horizontal radius of the bubble is varied from 1.0 to 5.0 km by 0.2-km increments, yielding 22 simulations.

4. Simulation results

Before analyzing dilution, it is useful to examine the bubble simulations to determine whether the convection produced is similar to what has been observed. Note the distinction between cloud and core, where "cloud" refers to any saturated volume and "core" refers to a saturated volume that is positively buoyant and moving upward (Dawe and Austin 2011a). The shell is defined here as any point that is part of the cloud volume and not part of the core volume. Note that this simple way of defining the cloud shell can potentially include downdrafts, overshooting thermals, and quiescent saturated regions. However, this caveat does not appear to affect the results presented here.

a. Cloud characteristics

The time versus height evolution of core and cloud buoyancy for a subset of the bubble simulations is shown in Fig. 1. We define buoyancy here using the virtual temperature T_v,

$$B = \frac{T_v - \overline{T_v}}{\overline{T_v}},$$

where the overbar indicates a horizontal average over the domain. Core buoyancy is always positive by definition and
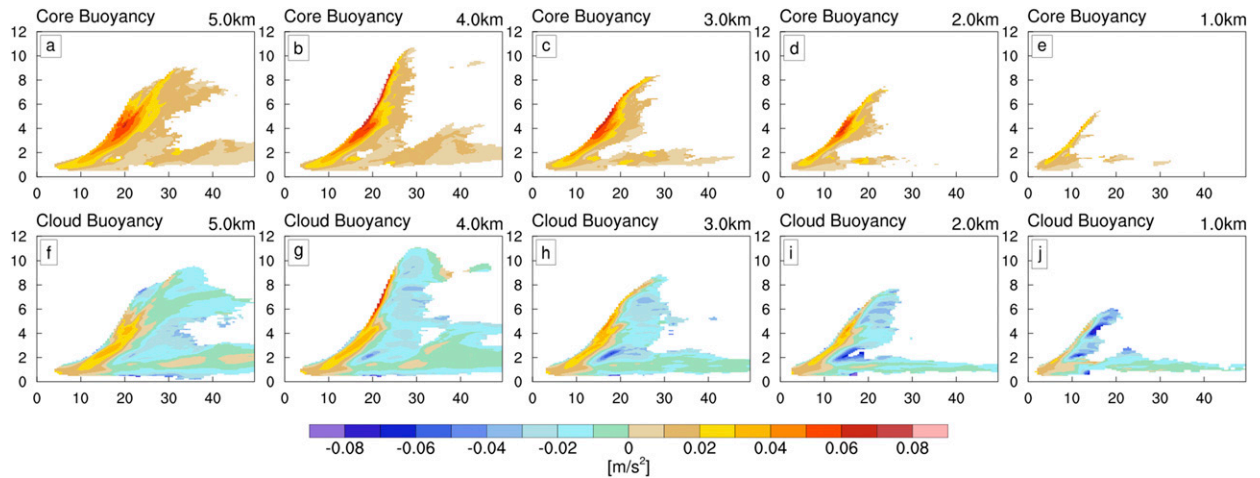
FIG. 1. Evolution of buoyancy for the (a)–(e) core and (f)–(j) cloud for select bubble simulations. The y axis shows height (km) and the x axis shows time (min).

does not exhibit much change in peak amplitude for bubbles with initial radii greater than 2 km (Figs. 1a–e). This is not surprising since the initial bubbles all have the same temperature and moisture perturbation. However, we might expect larger buoyancy for a wider cloud if we assume that entrainment or dilution is related to cloud radius.

Cloud buoyancy exhibits regions of strong negative buoyancy, especially in the cloud wake (Figs. 1f–j). A thin layer of negative buoyancy can be seen at times on the leading edge of the cloud, slightly above the cloud core. This suggests that evaporative cooling at cloud top is playing a role in the circulations of the thermal, which some have suggested may lead to cloud-top entrainment (Deardorff 1980; Stith 1992; Salzen and McFarlane 2002).

Cloud buoyancy is negative at the maximum height of the cloud, indicating that the cloud has overshot the level of neutral buoyancy.

Profiles of mean core vertical velocity show a range of 2–$4 \, \mathrm{m \, s^{-1}}$ in the midtroposphere (Fig. 2a). Maximum core velocities are found from 10 to $20 \, \mathrm{m \, s^{-1}}$ across the simulations (Fig. 2b). The range of updraft velocities is consistent with updraft statistics from in situ aircraft measurements (LeMone and Zipser 1980; Jorgensen and LeMone 1989; Lucas et al. 1994), as well as estimates derived from radar and satellite data (Uma and Rao 2009; Schumacher et al. 2015; Luo et al. 2014).

To further validate the realism of the simulations, we can compare the width of convection to observations. To
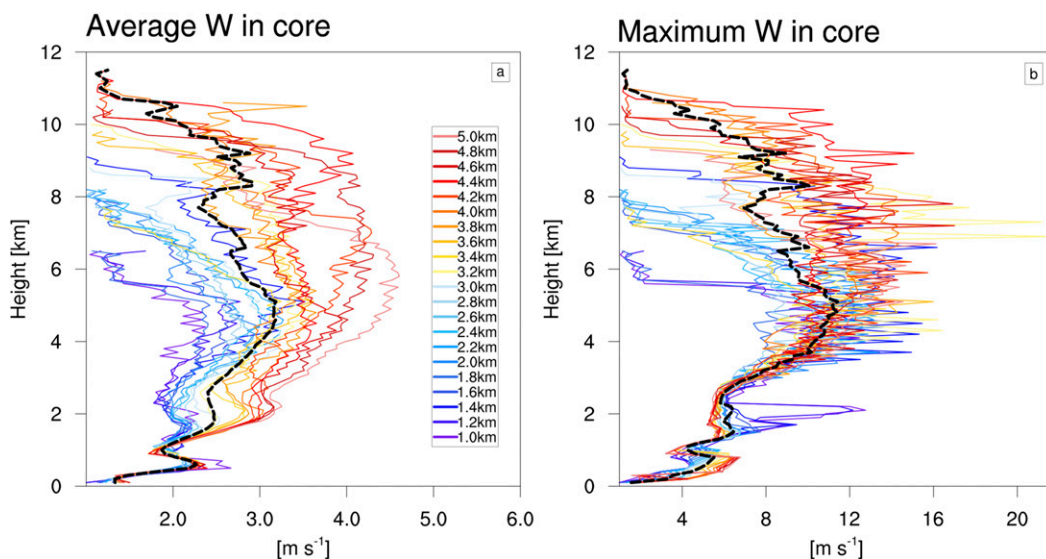

FIG. 2. Time-mean profiles of (a) average and (b) maximum vertical velocity in the core.
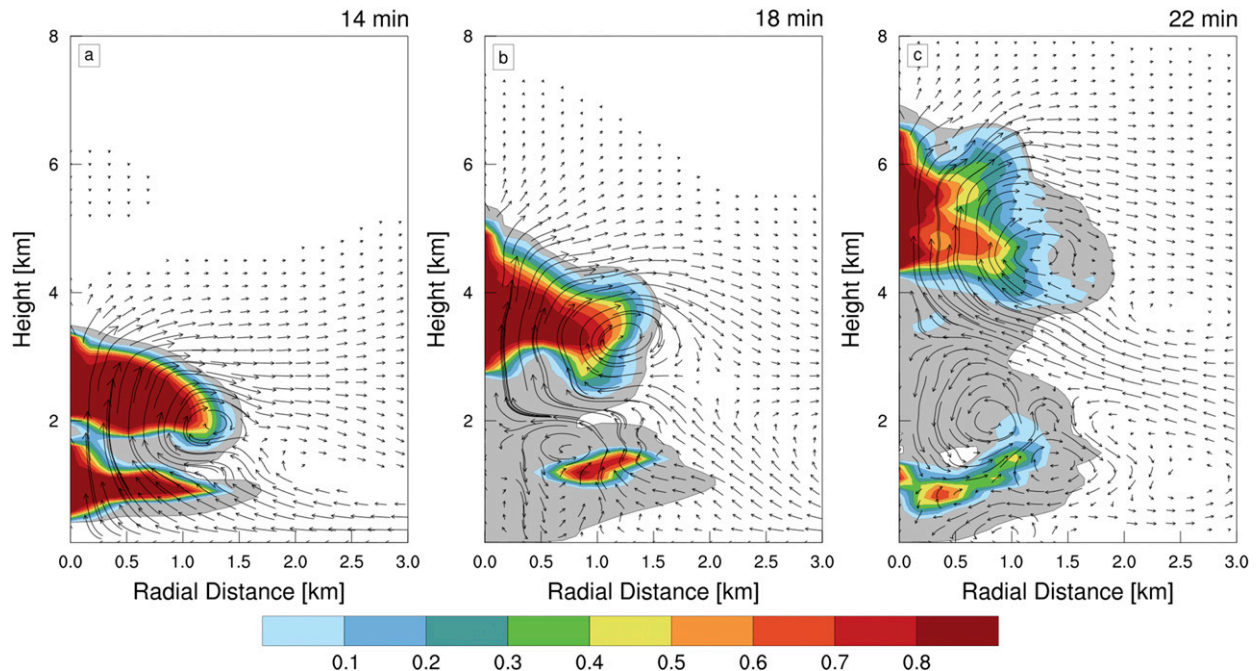
FIG. 3. Azimuthally averaged core volume fraction (colors) and circulation at (a) 14, (b) 18, and (c) 22 min of simulation time from the 4-km bubble. Gray shading indicates an azimuthally averaged cloud fraction of at least 0.1.

estimate the horizontal radius of a convective element, we use the method of Khairoutdinov and Randall (2006). After identifying the center of a feature, the outward radial distance r_i to the edge of the feature is measured along eight vectors spaced at equal angles around the centroid. The effective cloud radius R is then calculated as the root-mean-square of these measurements:

$$R = \sqrt{\frac{1}{8} \sum_{i=1}^{8} r_i^2}.$$

The range of effective core and cloud radii are roughly 0.4–3.0 km. These radii are consistent with previous radar, satellite, and modeling studies of tropical maritime cumuli (LeMone and Zipser 1980; Williams et al. 1992; Rickenbach and Rutledge 1998; Igel and van den Heever 2015; Hernandez-Deckers and Sherwood 2016).

b. Cloud circulation and shell

The cloud shell is a volume of saturated air that envelopes the core and is produced by detrained core air (Dawe and Austin 2011b). The shell can be variable in space and time, so it is not easy to characterize, but by azimuthally averaging the data, we can effectively filter some of this noise and characterize the shell in the height versus radius plane. Snapshots of the azimuthally averaged core (colors) and cloud (gray shading) fraction and circulation vectors from the 3.6-km bubble are shown in

Fig. 3 at 14, 18, and 22 min of simulation time. At 14 min, the convection has grown to an altitude of approximately 4 km and a shell has formed (Fig. 3a). Air is entraining through the shell but also coming up through the center of the updraft from the boundary layer. At 18 and 22 min, the core is cut off from the boundary layer and maintains a strong circulation, which drives entrainment laterally and from below the level of the core. The circulation during the growth of the cloud is reminiscent of a toroidal circulation as discussed in previous studies (Zhao and Austin 2005; Sherwood et al. 2013; Romps and Charn 2015). Note that while the azimuthally averaged flow appears laminar, the actual three-dimensional (3D) flow is much more turbulent.

From an azimuthally average perspective, entrainment and detrainment appear to be associated with coherent circulations, with inflow slightly below the rising thermal and outflow at cloud top. The strength of this circulation increases in larger clouds with stronger updrafts (not shown), suggesting both larger entrainment and larger detrainment. In this sense, the shell appears to act as a *conditioning* stage for the entraining air, such that it can mix with the previously detrained core air. We can grossly estimate the effective thickness of the shell with the difference of the cloud and core radii that was estimated previously,

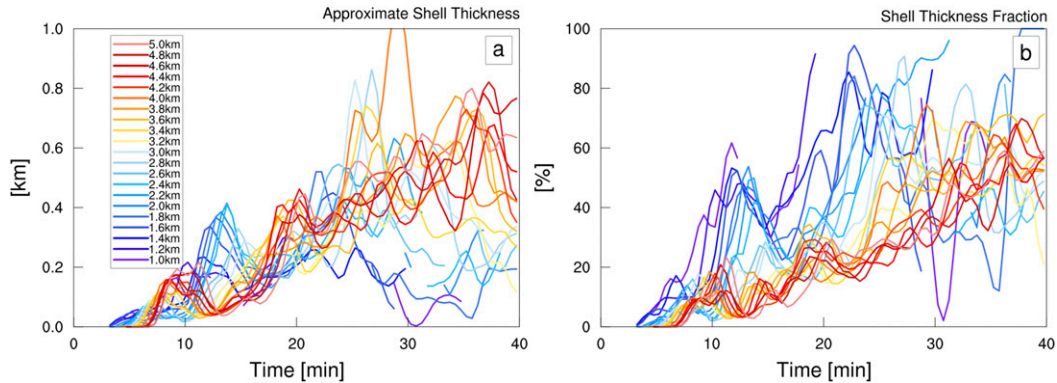$$R_{\mathrm{sh}} \approx R_{\mathrm{cld}} - R_{\mathrm{cor}} \qquad (15)$$

FIG. 4. Time series of the (a) approximate cloud shell thickness and (b) shell thickness fraction for the bubble simulations (see text).

and then average vertically. Shell thickness steadily increases at a similar rate over the cloud lifetime (Fig. 4a). Although the shell thickness is similar for the various bubble sizes, the shells of larger clouds are proportionally smaller when normalized by the cloud radius to give a fractional shell thickness (Fig. 4b).

c. Entrainment and detrainment

Entrainment and detrainment are often normalized by the vertical mass flux to obtain a fractional value that has units of per kilometer. This normalization can be problematic when the mass flux is small, so data is omitted here when the vertical mass flux falls under a threshold value of $10^{-1}\,\mathrm{kg\,m^{-2}\,s^{-1}}$. Figures 5a and 5b show the time-average profiles of fractional core entrainment and detrainment from each simulation, as well as ensemble-mean profiles in black. Large entrainment combined with small mass flux result in large fractional entrainment near the cloud base. Detrainment is much larger than entrainment in the troposphere, which shows that the thermal cores are shedding mass as they ascend. Data for the entire cloud volume show similar magnitudes of entrainment (Fig. 5c) but smaller values of detrainment (Fig. 5d), which suggests that the core is detraining into the cloud. The magnitudes of fractional entrainment are larger than that used in conventional parameterizations (Tiedtke 1989; Chikira 2010), consistent with the results of Romps (2010).

5. Dilution results

We will now explore convective dilution using proportional tendencies estimated with the method described in section 2. The calculation of terms in (14) can become erratic when cloud volumes are almost completely dilute, so to avoid this issue, data are excluded when the cloud average anomaly is less than 0.1 K for moist static energy ($h = c_p T + gz + L_v q_v$) and liquid–ice

static energy ($h_L = c_p T + gz - L_c q_l - L_f q_i$) and less than $0.1\,\mathrm{g\,kg^{-1}}$ for total nonprecipitating water q_t. Estimating the proportional tendencies can also be problematic when the cloud volume is very small. To avoid this issue, the calculation is limited to when the volume of interest contains a minimum of four full grid cells. The proportional detrainment tendency provides an additional challenge because the mass detrainment can be large enough to deplete the volume in a single model time step. This gives very large outlier dilution rates that can complicate the analysis, although they are not necessarily unphysical. To avoid complications from these outliers, a limit on the dilution time scale for detrainment is imposed so it cannot be shorter than 2 s (i.e., $30\,\mathrm{min^{-1}}$). The sensitivity of the proportional tendencies was rigorously examined, and although the quantitative values can occasionally be erratic without these thresholds, the ensemble-mean values are surprisingly robust, and thus, the conclusions are not affected.

Figure 6 shows profiles of the proportional tendencies due to entrainment of h, h_L, and q_t for both core and cloud. Profiles from individual bubble simulations are shown in thin colored lines according to the legend in Fig. 2, and the ensemble-mean profile is shown in the thick black line. The proportional tendencies are expected to be zero at cloud base, and while they are near zero above the cloud base, this is not the case at the level of the cloud base. This discrepancy is likely related to the unnatural way the bubbles are initiated. A few instances of positive proportional entrainment tendencies are observed, especially for h_L around 2–3 km, which indicates entrainment is enhancing the cloud properties at these levels rather than diluting them. At higher altitudes, entrainment is responsible for stronger dilution, which is likely related to the fact that the air is drier aloft but is also related to the fact the updrafts tend to be stronger (see Fig. 15).
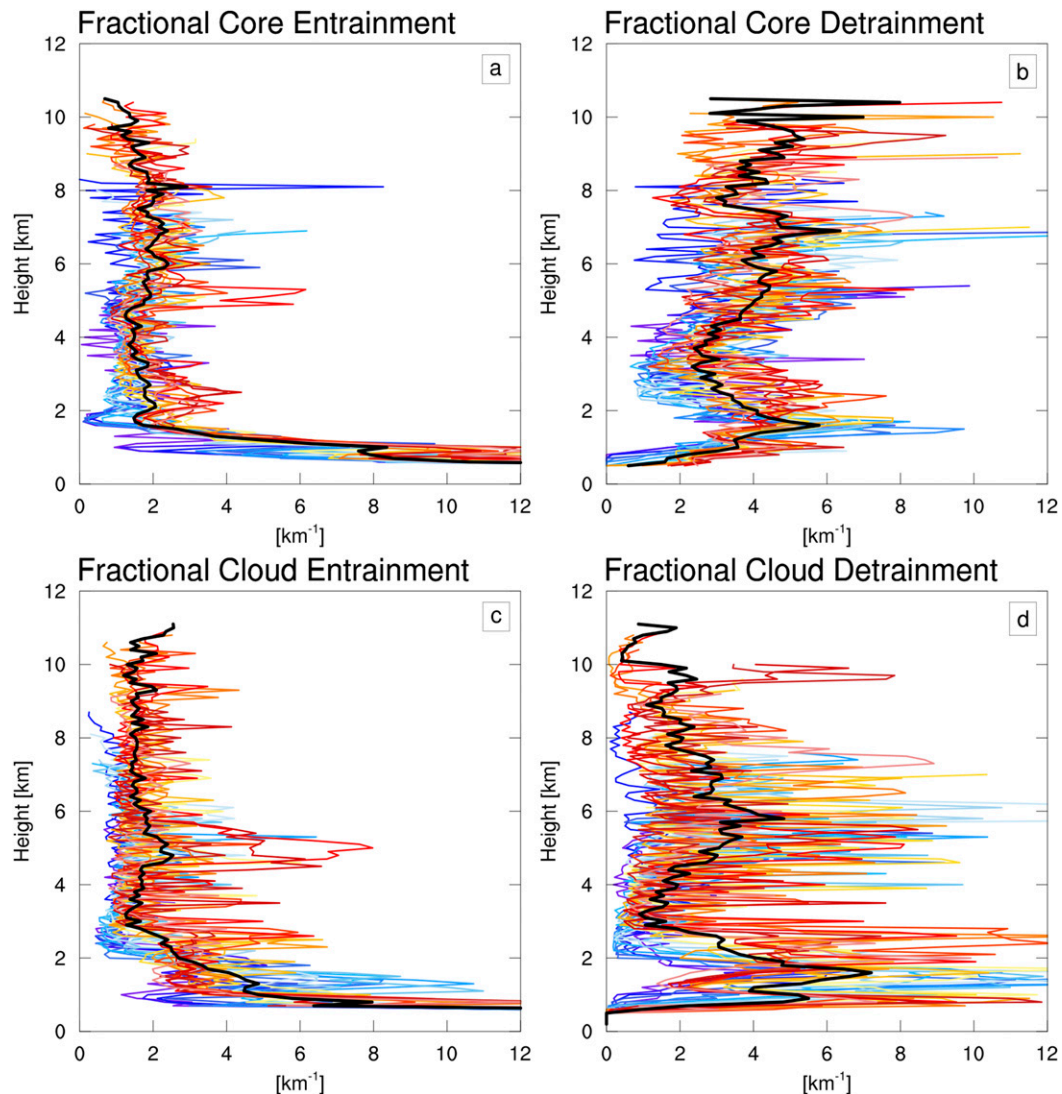
FIG. 5. Time-mean profiles of fractional (a),(c) entrainment and (b),(d) detrainment rates for (a),(b) core and (c),(d) cloud volumes colored according to the legend in Fig. 2. Black lines show ensemble means.

Comparing the dilution by entrainment between core and cloud, the core is less diluted by entrainment at lower levels, but at higher levels, the core is diluted by entrainment at a stronger rate compared to the cloud. This is likely because the core volume becomes progressively smaller as it reaches the level of neutral buoyancy and is easier to dilute with a given amount of entrainment.

To put the dilution by entrainment in a broader context of dilution by other processes, we can calculate the other terms of (14). For simplicity, the left-hand-side terms are added together to obtain a net dilution (Figs. 7a,e), and the dilution by all sources and sinks are estimated as a residual (Figs. 7d,h). The net proportional tendency is stronger than entrainment dilution of h_L and

q_t, but is comparable for h. The strong net dilution and associated large residuals suggest that these tracers are significantly affected by sources and sinks, such as radiative heating and hydrometeor fallout. The definition of h does not include hydrometeors, so it is not affected by fallout, but it does experience a source from the latent heat of freezing at upper levels, consistent with a smaller residual dilution. On the other hand, the definition of h_L subtracts the mass of hydrometeors scaled by their latent heat, so a loss of hydrometeors would increase the value of h_L (i.e., a smaller anomaly) and provide a residual source of dilution. Thus, it seems reasonable that fallout contributes the majority of the residual tendency. Attempts to verify this with the current model data were unsuccessful. Substantial modifications to the model are
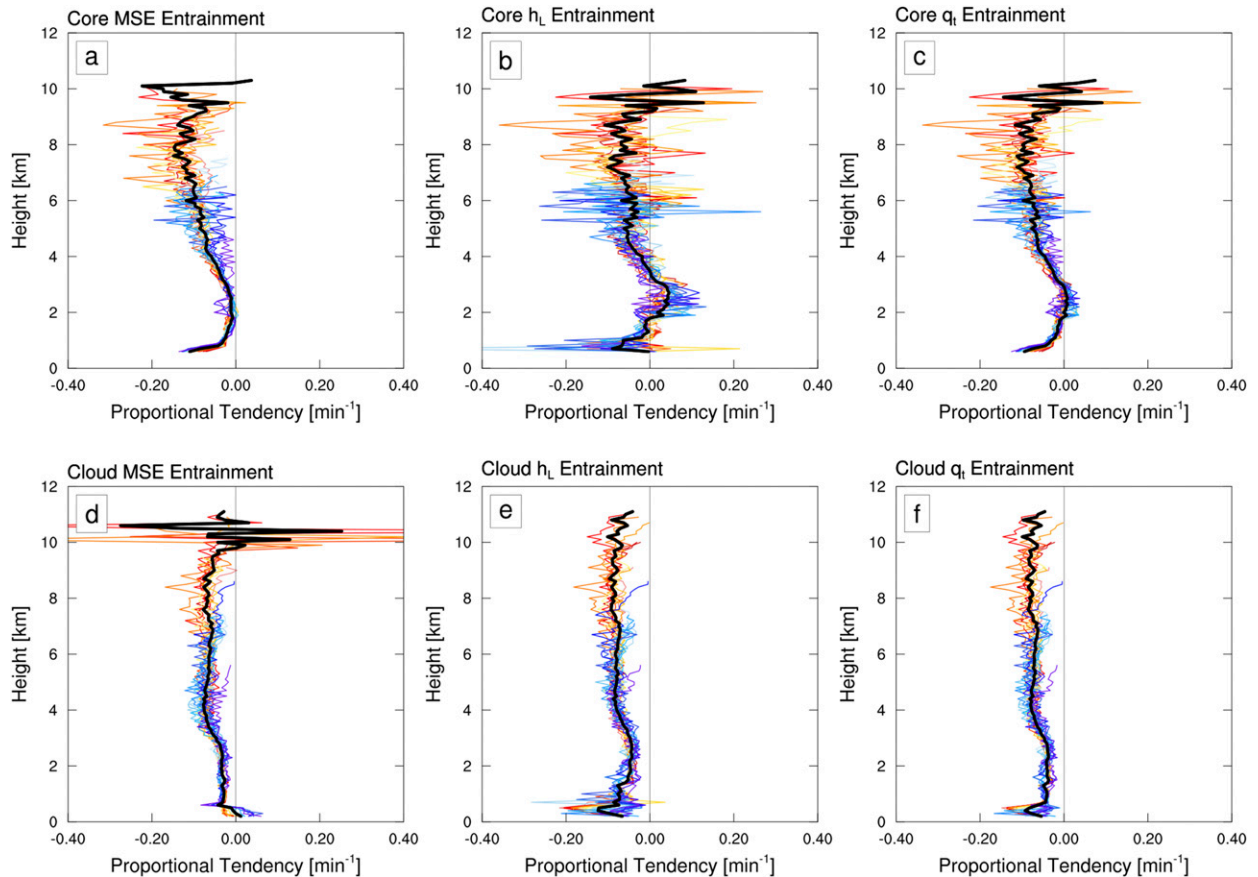
FIG. 6. Ensemble-mean profiles of (a)–(c) core and (d)–(f) cloud proportional tendency by entrainment (thick black lines) for (a),(d) h, (b),(e) h_L, and (c),(f) q_t. Colored lines show time-averaged profiles for individual bubble simulations according to the legend in Fig. 2.

needed to obtain the appropriate output data that would allow a more in-depth understanding of the residual dilution.

Detrainment contributes a positive proportional tendency, counteracting the dilution by entrainment (Figs. 7c,g). This indicates that detrainment acts to *concentrate*, or enhance, the cloud and also suggests that the least buoyant parts of the cloud are preferentially detrained. Interestingly, the effect of detrainment on the entire cloud volume is smaller for h at upper levels, but it is unclear how to interpret this result. Overall, entrainment is a nontrivial factor in the total net dilution above 4 km, although this is balanced by the effect of detrainment and overwhelmed by source/sink processes.

Inverting the proportional tendencies due to entrainment and detrainment in Fig. 7 yields a dilution time scale of approximately 5–20 min, which is on the order of the lifetime of the main core of the bubble convection. Some convective parameterizations that employ a spectrum of entraining plumes only consider detrainment at the top of the cloud (Moorthi and Suarez

1992), but the results here suggest that the effects of detrainment below the terminal height should not be ignored. Similarly, the effects of sources and sinks can inflict a dilution time scale as low as a few minutes. In the case of moist static energy, the smaller residual suggests that neglecting these sources and sinks may be less of a concern.

a. Does horizontal scale influence dilution?

Many simple cloud models and convective parameterizations explicitly or implicitly assume that entrainment is inversely proportional to cloud radius (Morton et al. 1956; Levine 1959; Simpson 1971; Arakawa and Schubert 1974; Tokioka et al. 1988; Wagner and Graf 2010; Stirling and Stratton 2012). This assumed relationship is often expressed as

$$\mu = \frac{\alpha}{R}, \qquad (16)$$

where μ is the fractional entrainment rate, R is radius, and α is a coefficient of proportionality.
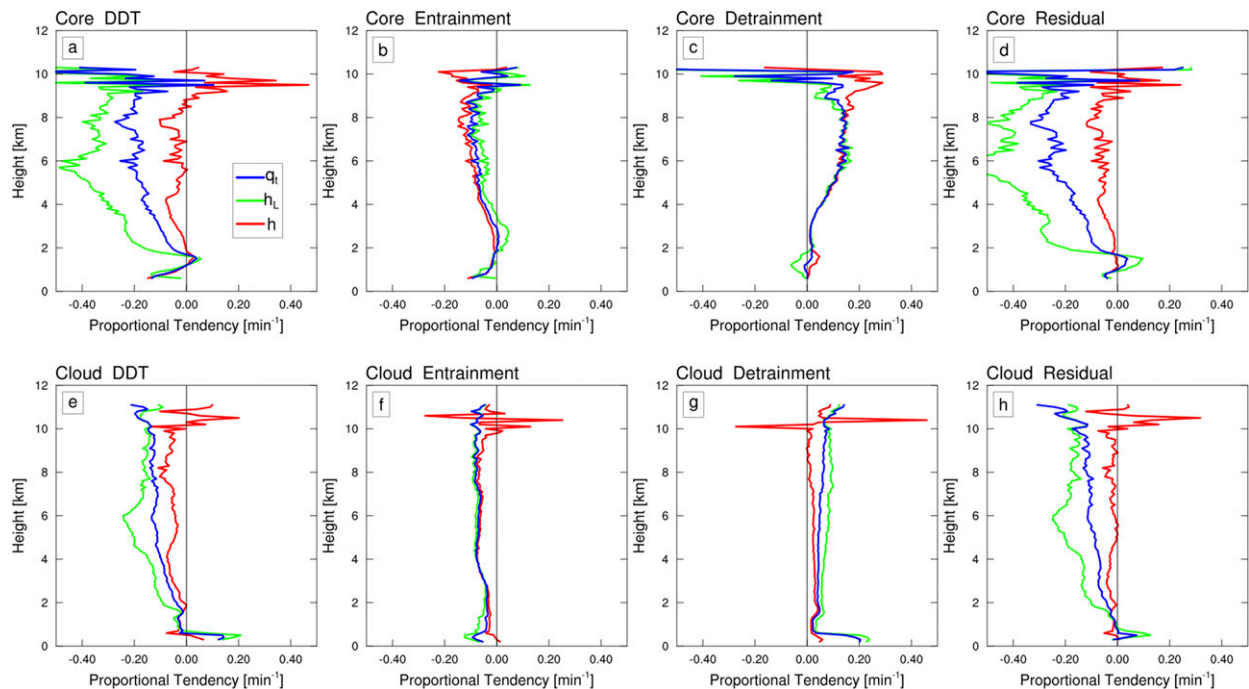
FIG. 7. Ensemble-mean profiles of the proportional tendencies from all terms in (14) in both (a)–(d) core and (e)–(h) cloud volumes and for total water (blue), liquid–ice static energy (green), and moist static energy (red). (a),(e) The left-hand-side terms of (14) are shown as a sum for brevity. (d),(h) The residual includes all source and sink terms.

Attempts to verify (16) with observations generally support an inverse relationship (Sloss 1967; McCarthy 1974; Lu et al. 2012), but these studies rely on other assumptions, such as negligible detrainment. On the other hand, Dawe and Austin (2013) used the direct measurement technique and found compelling evidence that entrainment is *directly* proportional to cloud area in the case of shallow convection.

The systematically varying initial radii of the bubble experiments here allow a direct test of this idea in the context of deep convection. Figure 8 shows scatterplots of fractional core entrainment and proportional entrainment tendencies of h_L and q_t against core radius. Data below 3 km are excluded to avoid the initial thermal formation. Thick dotted lines show binned averages, and green lines show the result of linear least squares fit, which are statistically significant at the 95% confidence level. The fractional entrainment data in Fig. 8a are not consistent with the inverse relationship in (16). On the other hand, the proportional entrainment tendencies indicate decreasing dilution with increasing radius on average (Figs. 8b,c), although there is a lot of scatter in the data. Similar results can be found for the cloud volume (not shown). Although the relationship between dilution and radius does not explain much of the variation in dilution, it appears that the use of the inverse radius assumption in (16) is somewhat justified for conventional convective

parameterizations. The lack of a strong relationship here suggests that there are better ways to formulate entrainment for cumulus parameterizations.

b. Maximum dilution

The classic entraining plume is designed such that the entrained air is assumed to be identical to the far-field, cloud-free environment. The dilution metric here allows us to estimate a theoretical maximum core dilution that would occur if this were the case. This is done by simply modifying the numerator of the entrainment term in (14).

Figure 9 shows the ensemble-mean proportional tendency of h_L and q_t by entrainment (solid) compared to the theoretical maximum tendency (dashed) for both core (red) and cloud (blue) volumes. As expected, the maximum proportional core tendencies are much more negative, corresponding to a shorter dilution time scale of 2–5 min, roughly. The maximum cloud proportional tendency is only slightly more negative because the outer portion of the cloud is not buffered from the ambient environment. Large values near cloud base are simply due to how the bubbles are initiated.

The difference between the actual and maximum core dilution highlights the role of the cloud shell to buffer the core against dilution by entrainment. Averaging across the shell volume shows that q_t in the shell is well
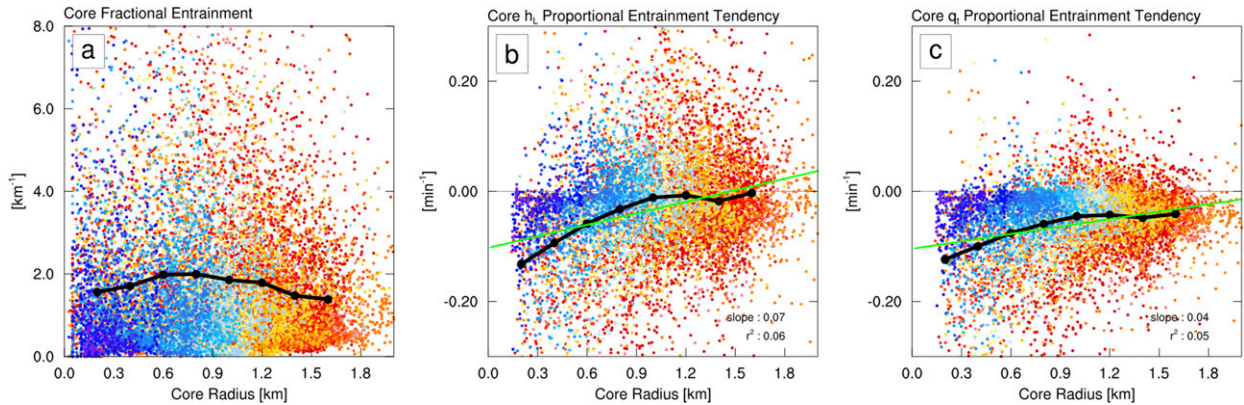
FIG. 8. Scatterplot of (a) fractional core entrainment and proportional core entrainment tendencies of (b) h_L and (c) q_t against core radius (colored according to the legend in Fig. 2). Data below 3 km are excluded. Binned averages of the data are shown as the black line. The green lines are the result of a linear least squares fit, which are significant at the 95% confidence level.

correlated with that of the air entraining into the core (Fig. 10a), both of which are wetter than the ambient environment. Restricting the definition of the shell to negatively buoyant cloud air gives a similar result (Fig. 10b).

The shell air appears to provide a decent predictor of the properties of air entrained into the core, so then does the amount of shell air affect dilution? Figure 11 shows the proportional core entrainment tendencies of h_L and q_t against the fractional shell volume, defined by dividing the shell volume by the total cloud volume at each time and height. There is a clear increase of proportional entrainment tendencies from negative to positive on average as the shell becomes large relative to the cloud. Linear regression also reveals a statistically significant positive

relationship at the 95% confidence level. The differences between h_L and q_t are likely due to how each is affected by hydrometeor sedimentation and radiative heating. Data below 3 km are excluded, and including these points makes the relationship less robust. This result further shows how the shell acts to buffer the core against dilution by entrainment as the thermal ascends through the troposphere. This conclusion is essentially equivalent to that of Romps (2010), who showed that assuming a cloud entrains air directly from the ambient environment systematically biases the estimate of entrainment rate to be low.

c. Entrainment versus dilution

The proportional tendency due to entrainment is generally negative, indicating dilution (Fig. 9), but to
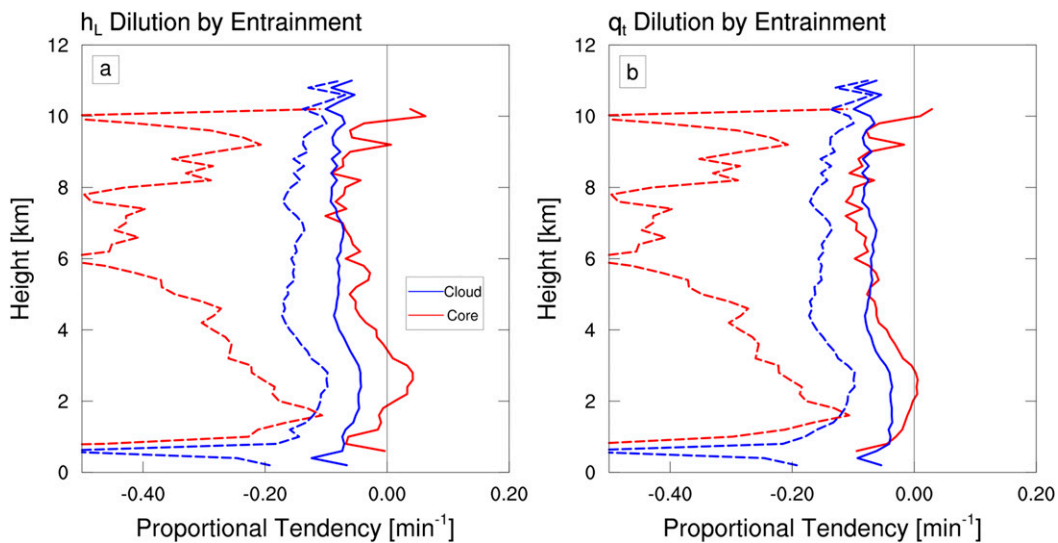

FIG. 9. Ensemble-mean profile of proportional tendencies due to entrainment (solid) and the theoretical maximum core dilution (dashed; see text) for (a) h_L and (b) q_t.
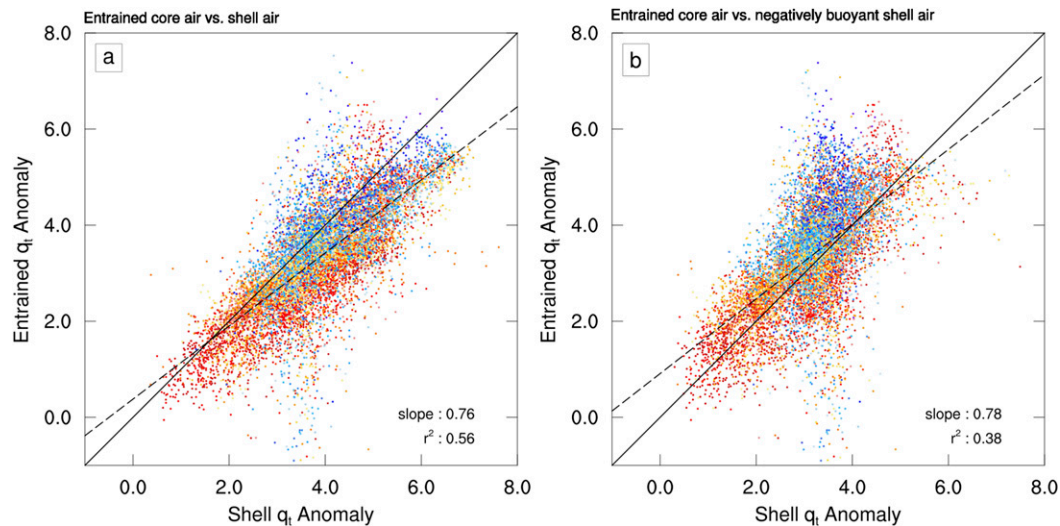
FIG. 10. Scatterplot of total water anomalies for (a) entrained core air vs shell air (colored according to the legend in Fig. 2). (b) An alternate definition of the cloud shell (see text). The thin black line shows the unity line, and the dashed line shows the results of linear regression analysis.

what extent are entrainment and dilution related? According to (14), more entrainment should cause more dilution if all other terms are constant. However, we know this is not the case at low levels (Figs. 5,6). A direct comparison of entrainment and dilution by entrainment of h_L for core and cloud volumes is shown in Fig. 12. In both cases, the strongest proportional tendencies correspond with the weakest entrainment rates, and vice versa, suggesting no general relationship between entrainment and dilution.

By repeating the analysis in Fig. 12, omitting data below 3 km and coloring the points by the fractional shell volume, we get a different picture of how entrainment and dilution are conditionally related (Fig. 13). If we only consider data with a shell fraction below some cutoff, such as 0.3, we can obtain a statistically significant relationship between entrainment and dilution (not shown). Due to the subjective nature of this conditional relationship, the linear regression analysis has been omitted here, but from this result, we can conclude that
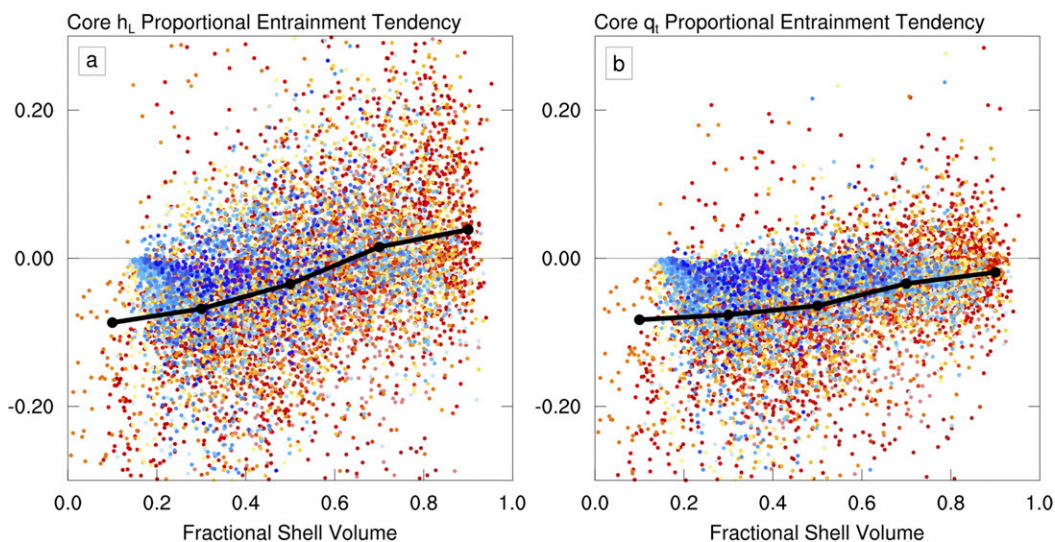

FIG. 11. Scatterplot of core proportional tendency due to entrainment for (a) h_L and (b) q_t against fractional shell volume. Data below 3 km are excluded. Data are colored according to the legend in Fig. 2. Binned averages of the data are shown with the black line.
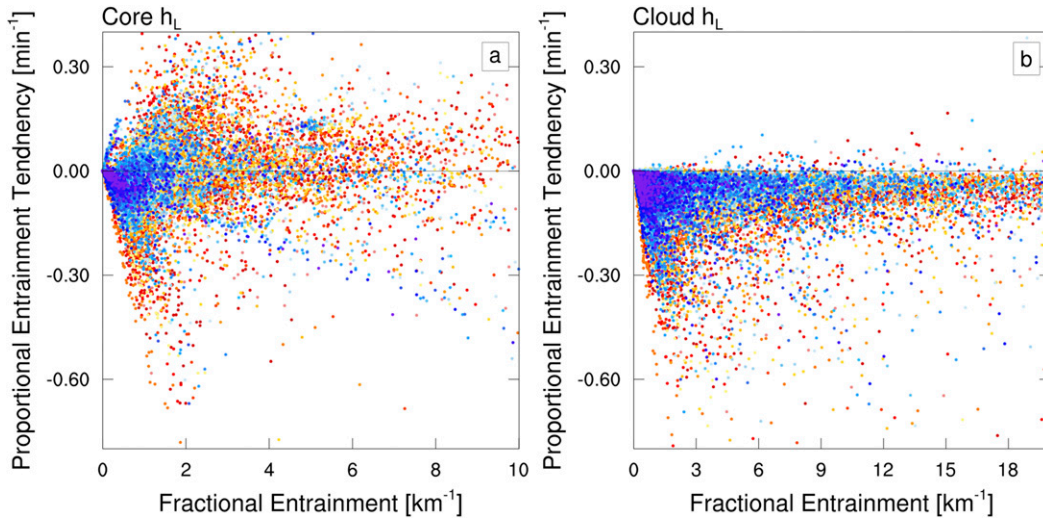
FIG. 12. (a) Core and (b) cloud proportional tendencies due to entrainment against core and cloud fractional mass entrainment for h_L colored according to the legend in Fig. 2.

more entrainment causes more dilution as long as the shell is sufficiently thin.

Some formulations of entrainment are based on vertical velocity (Chikira and Sugiyama 2010), so it is interesting to repeat the analysis of Fig. 13 but coloring the data by the core updraft velocity (Fig. 14). As before, we can obtain a statistically significant relationship between entrainment and dilution by restricting the data to instances with an updraft velocity of at least $8\,\mathrm{m\,s^{-1}}$ (not shown). This suggests that entrainment and dilution are also related when the updraft is sufficiently strong. Figure 15 shows how entrainment and h_L dilution by

entrainment are each related to core velocity. All quantities exhibit a clear relationship with core velocity, although it is unclear how a theoretical relationship would be formulated. The binned averages (dotted black lines) show that entrainment strongly decreases with increasing core velocity up to around $7\,\mathrm{m\,s^{-1}}$ (Figs. 15a,b). Dilution by entrainment decreases with increasing core velocity in both core and cloud (Figs. 15c,d). Similar results are found for dilution of q_t.

The results in Figs. 13 and 14 suggest that the shell volume and core velocity may be related, which is an unexpected result. Figure 16 compares these quantities
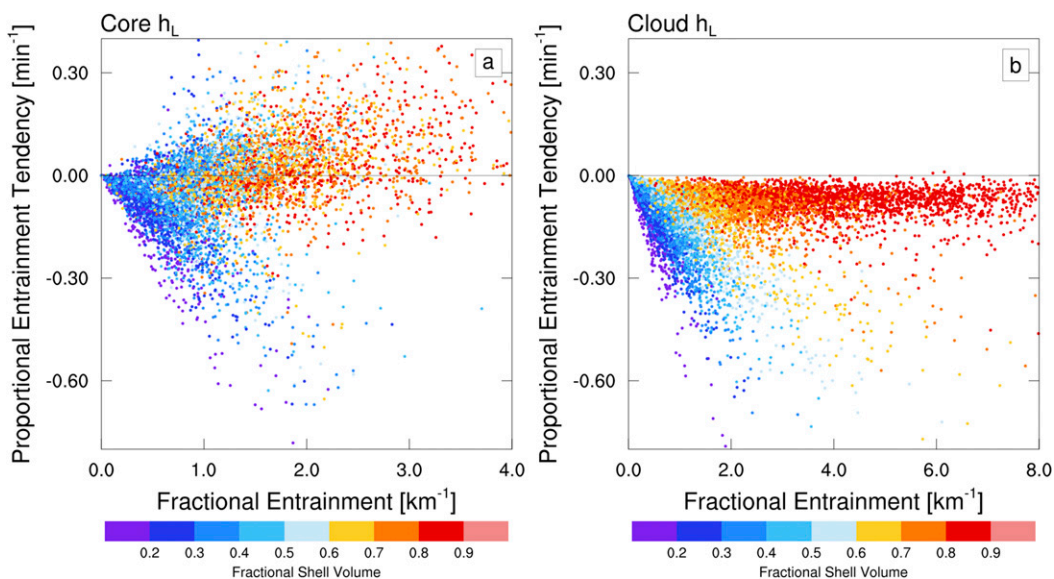

FIG. 13. As in Fig. 12, except data are colored by fractional shell volume. Data below 3 km are excluded.
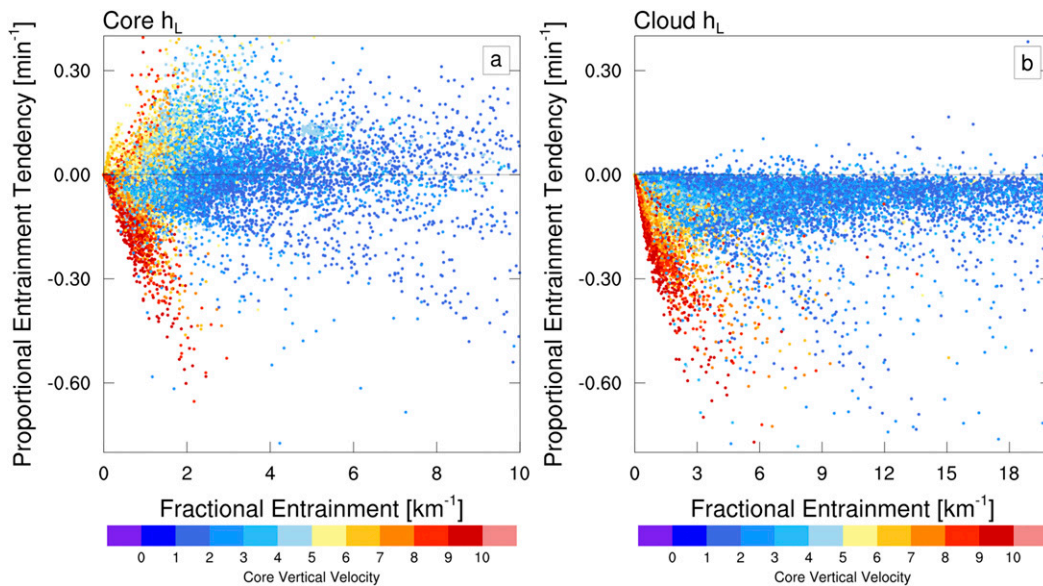
FIG. 14. As in Fig. 12, except data are colored by core vertical velocity.

directly, excluding data below 3 km, and reveals a statistically significant relationship, in which fractional shell volume decreases for stronger updrafts. We can understand this result a bit more by building composite thermals with different vertical velocities. To do this, the height of the thermal at each time is determined as the highest local maximum of core mass flux, which is a smoother function of height than vertical velocity. The data were then azimuthally averaged before compositing. Cores are excluded when their centers are below 3 km. Figure 17 shows composites for updraft velocities of 4, 6, and 8 m s^{-1}, with a threshold of ± 1 m s^{-1}. The core volume as a fraction of the cloud volume (i.e., core fraction) is shown in colors, and the cloud volume as a fraction of grid volume is shown in contours. As core velocity increases, the toroidal circulation becomes stronger at the cloud edge, and the core occupies a larger portion of the thermal This suggests that the relationship in Fig. 16 is simply a reflection of the fact that a stronger updraft produces more condensational heating, which increases the buoyancy of the thermal and naturally results in a larger core volume and smaller shell volume. This leaves the core volume more exposed to dilution from the air from the cloud-free environment.

6. Resolution sensitivity

Model grid spacing sets a lower limit on the spectrum of turbulence that can be explicitly resolved and affects the amount of turbulent entrainment, and possibly dilution. The convection produced in the bubble simulations exhibits circulations on the scale of the thermals themselves, but smaller-scale turbulent mixing contributes to the total entrainment. Some parameterizations artificially employ a separation of entrainment into "organized" and "turbulent" components (Tiedtke 1989), but it is unclear how one would separate the directly measured entrainment and see how these components affect dilution. Alternatively, we can change the grid spacing to examine the effect of resolving more or less turbulent kinetic energy. Reproducing the bubble experiments at a higher resolution is prohibitively expensive with current resources, so testing the effect of a coarser resolution is more practical. Additional bubble simulations with a grid spacing of 200 m were conducted with identical domain size and initialization.

Figure 18 shows a comparison of ensemble-average profiles of mass flux, vertical velocity, core volume, and shell fraction for bubble simulations with 100- (solid) and 200-m (dashed) grid spacing. Similar results can be found for the entire cloud volume (not shown). The convection with larger grid spacing has a smaller mass flux above 2 km but a slightly stronger updraft velocity on average, which is contrary to the findings of other studies (Varble et al. 2014). The core volume is systematically smaller above 2 km with coarse resolution, which leads to a larger fractional shell volume. Figure 19 shows that core entrainment and detrainment are also systematically reduced with the 200-m grid. The same is found for the cloud volume (not shown). Reduced entrainment with larger grid spacing is expected since we have truncated the turbulence spectrum. The reductions of both entrainment and mass flux make the fractional entrainment virtually unchanged between the resolutions (not shown).
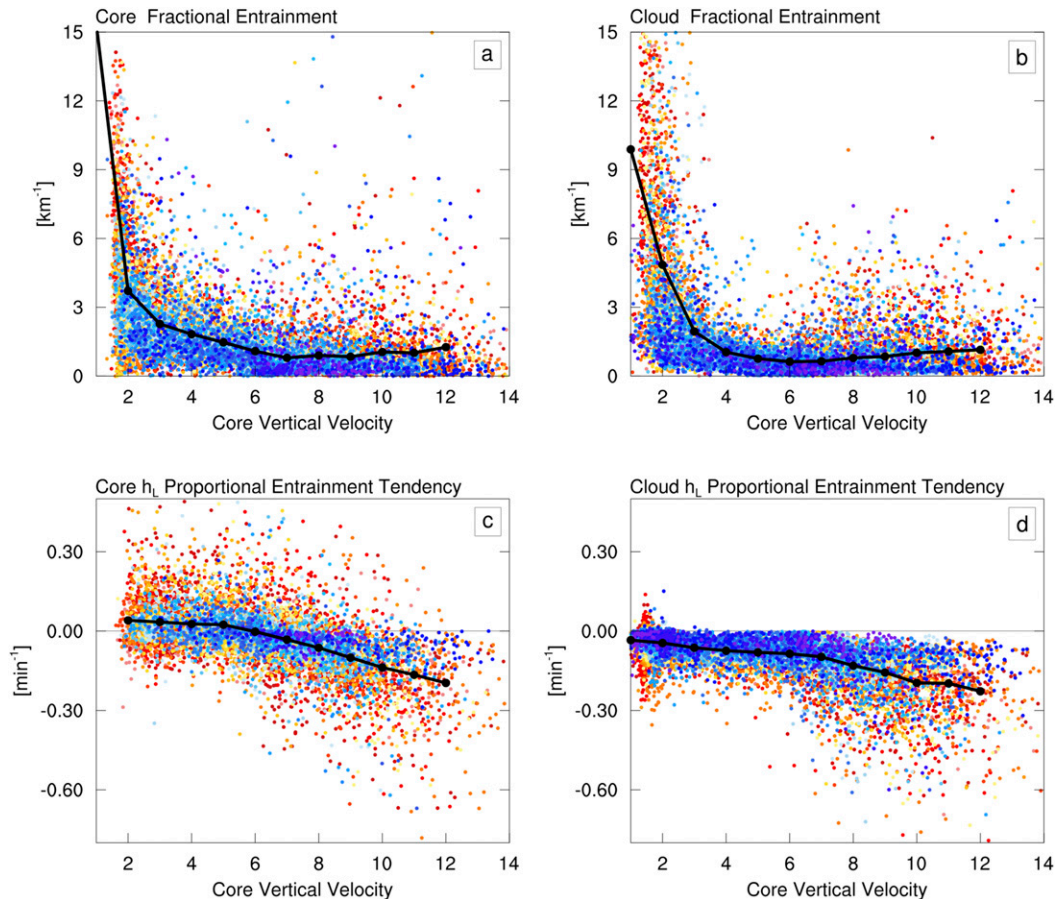
FIG. 15. Scatterplots of (a),(b) entrainment and (c),(d) dilution for (a),(c) core and (b),(d) cloud against core vertical velocity. The dotted black line shows binned averages. Data below 3 km are excluded.

Figure 20 shows ensemble-average profiles of core dilution (solid) and the maximum theoretical dilution (dashed) if there were no shell (see section 2b) for the 100- (black) and 200-m (green) simulations. The most striking difference between the simulations is that the maximum core dilution is strongly reduced with larger grid spacing. This is a result of reduced mass entrainment, since the ambient environment is the same in all simulations (Fig. 19).

Dilution by entrainment for both h_L and q_t is slightly stronger with a coarser resolution at certain levels. Black dots in Fig. 20 indicate where this difference is statistically significant at the 95% confidence level using the conventional Student's t test. It is difficult to understand these differences given the relationships that were hinted at by previous figures in section 5. To fully explore these results, it would be necessary to see whether these differences are representative of a general trend across a wider range of grid spacing, but this is beyond the scope of the present study.

7. A toy Lagrangian thermal with an explicit cloud shell

The results of section 5 suggest that the cloud shell plays a role in conditioning the air entrained into the core, thereby reducing the dilution by entrainment and allowing larger entrainment rates than those typically used in convective parameterizations. A toy model of a buffered Lagrangian thermal (BLT) with an explicit cloud shell is developed to test this notion in a simplified framework (see appendix). The BLT model describes the evolution of a buoyant spherical thermal with an explicit shell that functions as a passive thermodynamic buffer. The shell grows steadily, similar to the results in Fig. 4, as a mixture of detrained core air and entrained environmental air (see Fig. 21). Moist static energy ($h = c_p T + gz + L_v q_v$) is used here as the prognostic thermodynamic tracer from which other thermodynamic properties can be diagnosed. This choice avoids the complication of hydrometeors that comes with
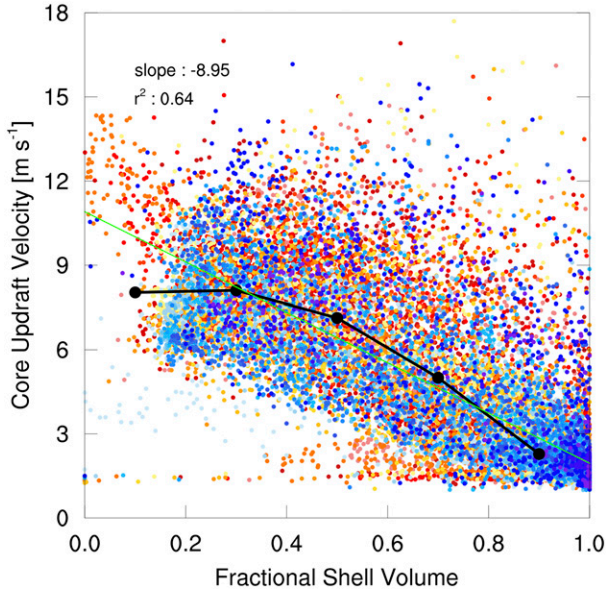
FIG. 16. Scatterplot of core vertical velocity against fractional shell volume. Data below 3 km are excluded.

the use of the liquid–ice static energy. The model prognostic equations for the thermal core and shell are as follows:

$$\frac{dm_c}{dt} = m_c(\varepsilon_c - \delta_c), \tag{17}$$

$$\frac{dm_s}{dt} = m_c[\varepsilon_s - \delta_s - (\varepsilon_c - \delta_c)], \tag{18}$$

$$\frac{dm_c w_c}{dt} = m_c(B - D), \tag{19}$$

$$\frac{dm_c h_c}{dt} = m_c(\varepsilon_c h_s - \delta_c h_c), \tag{20}$$

$$\frac{dm_s h_s}{dt} = m_c[\varepsilon_s \overline{h} - \delta_s h_s - (\varepsilon_c h_s - \delta_c h_c)], \tag{21}$$

where m is mass, w is vertical velocity, B and D are the net buoyant and drag accelerations of the thermal defined in (A10) and (A11) of the appendix, and ε and δ are the fractional entrainment and detrainment rates. Subscripts c and s indicate core- and shell-average quantities, respectively. The model is discretized using a simple Euler forward scheme with a small time step of 1 s to ensure computational stability. The shell component of the model can be easily disabled by setting the $h_s = \overline{h}$ at every time step.

The fractional entrainment rates in the above equations are expressed as mixing time scales ε_t (s^{-1}). To use the more familiar mixing length scale ε_z (m^{-1}), we can use the following relationship:

$$\varepsilon_t = \varepsilon_z w_c. \tag{22}$$

Although Fig. 15 and previous studies (e.g., Neggers et al. 2002) suggest entrainment can be formulated as a function of vertical velocity, it is unclear how best to formulate entrainment for the BLT model, so constant values of entrainment and detrainment will be used here for simplicity. Based on the fractional entrainment profiles in Fig. 5, the entrainment rates of the core and shell are set to 1.5 km^{-1}. Although detrainment rates are generally larger than entrainment in the bubble simulations (Fig. 5), the detrainment rate for the model is set equal to the entrainment rate initially. The model is initialized with a radius of 2 km, temperature perturbation
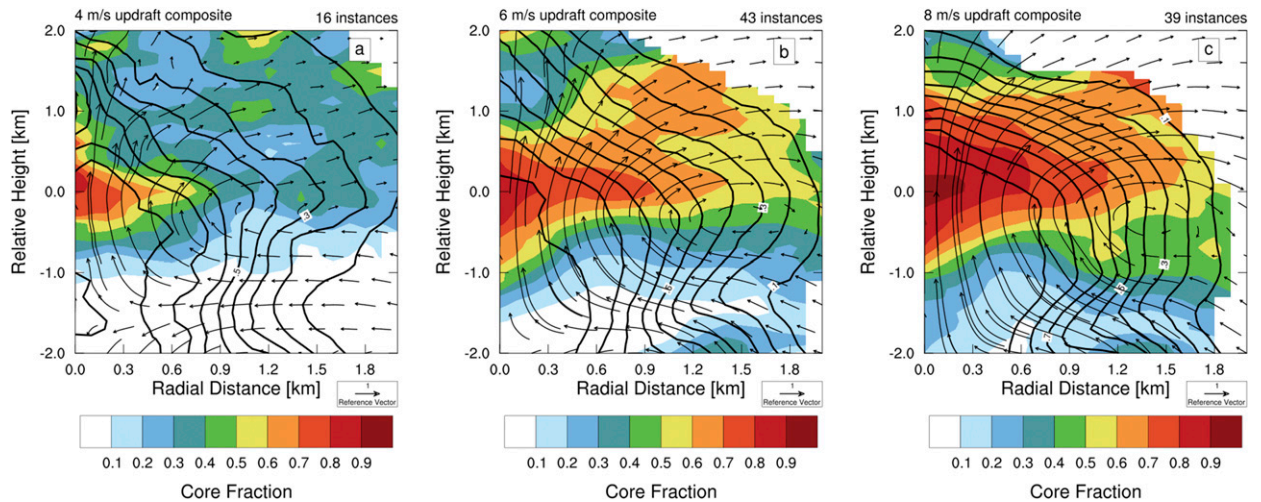

FIG. 17. Composites of azimuthally averaged core fraction (colors), cloud volume (contours), and circulation (vectors) for thermals with core updraft velocity of (a) 4, (b) 6, and (c) 8 m s^{-1} (see text).
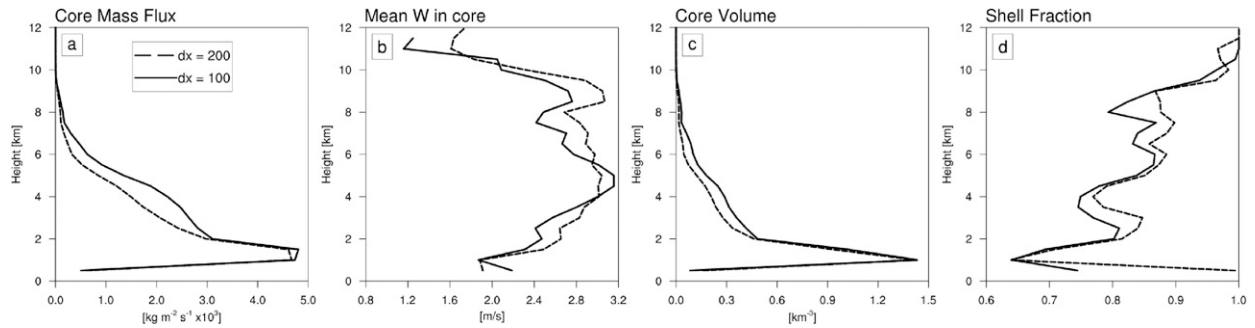
FIG. 18. Ensemble-mean profiles of (a) mass flux, (b) vertical velocity, (c) core volume, and (d) shell fraction for bubble simulation data with 100- (solid) and 200-m (dashed) grid spacing.

of 1 K, and moisture perturbation of $2\,g\,kg^{-1}$, similar to the bubble simulations with an initial perturbation radius around 4 km that reach a terminal height of 10 km (see Fig. 1b).

Figure 22 shows the evolution of core moist static energy (Fig. 22a) and time scale of dilution by entrainment (Fig. 22b) from the toy BLT model. Without a shell, the thermal can only reach an altitude of roughly 1 km (solid blue). When the shell component is enabled, the thermal can reach a higher altitude of 4 km (solid red), which is still below the terminal height of the bubble simulations. The dilution is initially similar to the case without a shell because of the time needed to build the shell mass. Alternatively, we can reach the same height without the shell if we lower the entrainment rate to $0.55\,km^{-1}$ (dashed blue), although the thermal takes a different "thermodynamic path" and exhibits more dilution from entrainment above the boundary layer.

An interesting aspect of the BLT model is that the shell provides a feedback to the core. If we increase the core detrainment rate by $0.2\,km^{-1}$ (dashed green), the thermal ascends significantly higher to around 8 km, which is closer to the bubble simulations. Increasing the detrainment further allows the thermal to ascend higher but also depletes the mass of the thermal faster.

Comparing the BLT dilution profiles in Fig. 22 with those from the bubble simulations in Fig. 6, we can see there is much more dilution in the BLT model. This is especially true in the lowest 2–3 km where the bubble simulations exhibit zero or negative dilution from entrainment. This discrepancy could be due to several factors since the toy model is missing many important processes, such as condensate loading and diffusion. Romps and Kuang (2010) showed that ice microphysics also play an important role in explaining how dilute convection can reach the upper
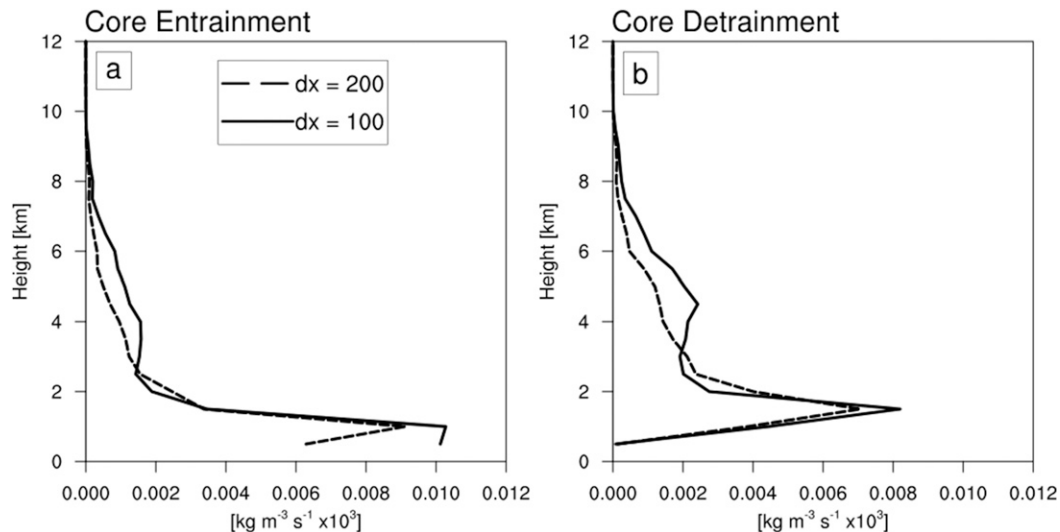

FIG. 19. As in Fig. 18, but for core (a) entrainment and (b) detrainment.
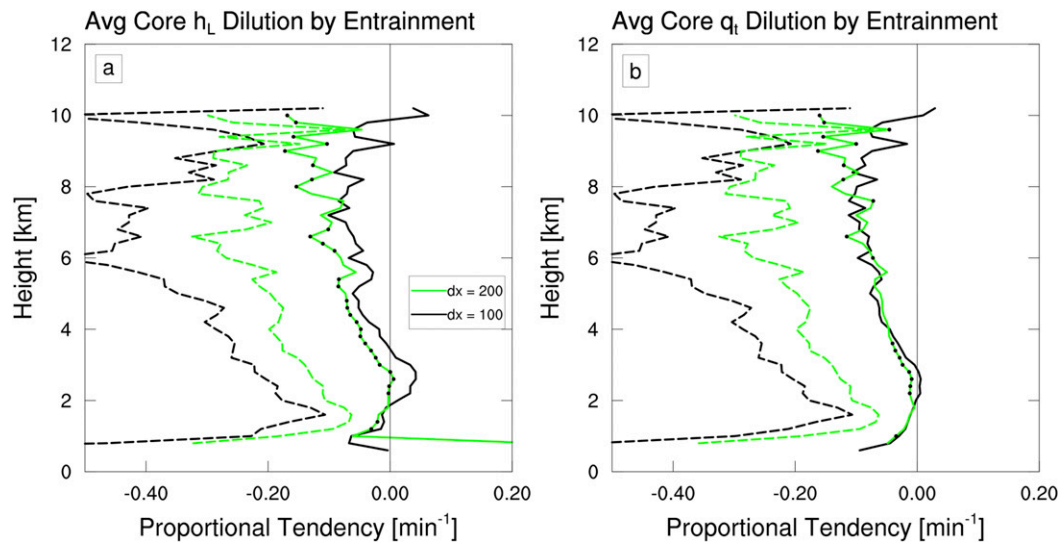
FIG. 20. Ensemble-mean profiles of (a) h_L and (b) q_t core dilution by entrainment (solid) and maximum theoretical dilution by entrainment (dashed) for bubble simulation data with 100- (black) and 200-m (green) grid spacing.

troposphere, which is another aspect missing from the BLT model. Additionally, the BLT is initialized with the assumption that the thermal is spherical, which certainly does not reflect the bubble simulations.

In spite of its oversimplified nature, the BLT model demonstrates how convection can reach high altitudes with large entrainment rates by recycling air from the humid layers around the core. The approach here provides a way to include explicit heterogeneity to a cloud model without adding much complexity (see also Sherwood et al. 2013) and may be useful for other experiments, such as adding a third component to account for nearby air that has been modified by previous convection. These results also show how the dilution time scale can be useful for comparing simplified models with explicitly simulated convection.

8. Conclusions and discussion

A method for estimating the dilution due to entrainment and detrainment with proportional tendencies is presented and applied to bubble simulations with a spectrum of initial radii from 1 to 5 km. The conclusions from this study can be summarized as follows:

- Entrainment generally acts to dilute convection, although its effect can be overwhelmed by the effects of detrainment and source/sink processes.
- Detrainment acts to enhance convection, which balances the dilution by entrainment.

- Dilution by entrainment exhibits a weak negative relationship with the horizontal scale of the convective element, whereas entrainment does not exhibit any such dependence.
- Core dilution by entrainment is significantly reduced by the presence of the cloud shell.
- Entrainment and dilution by entrainment are not well correlated except when the cloud shell is relatively thin or when the core updraft is sufficiently strong.
- Dilution estimates appear to be somewhat sensitive to model resolution, but it is unclear whether the differences are a systematic consequence of grid spacing.

The dilution metric discussed here offers a promising way to probe other question surrounding entrainment. For instance, Bechtold et al. (2008) formulated entrainment such that it decreases with increasing environmental humidity. Although they did not discuss the justification for this relationship, implementing it into a convective parameterization produced notable improvements. Recent studies by de Rooy and Siebesma (2008)
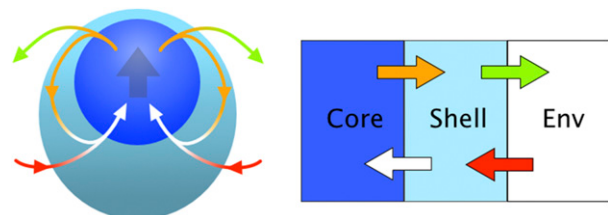

FIG. 21. Schematic diagram showing how a shell component of a rising thermal is treated explicitly in the buffered Lagrangian thermal model.
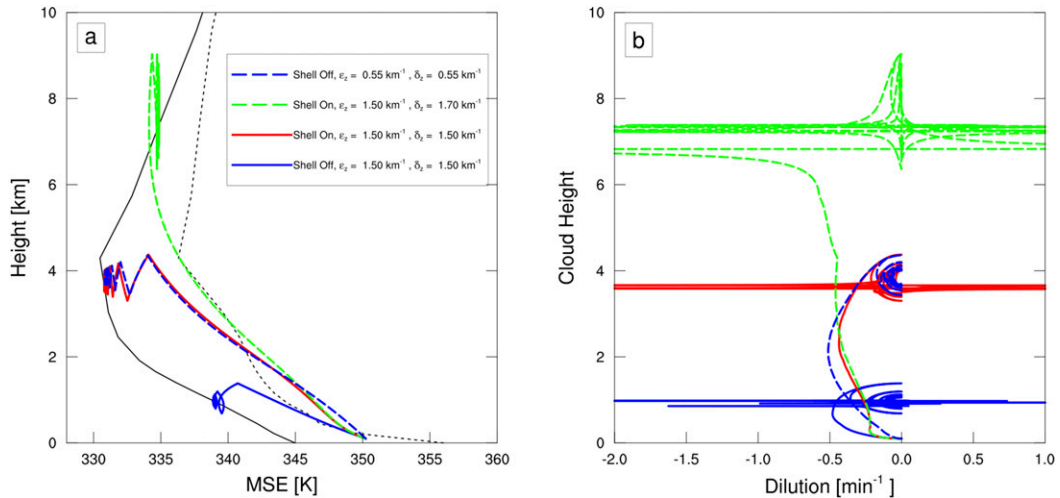
FIG. 22. Evolution of core (a) moist static energy and (b) dilution by entrainment from the toy BLT model using an entrainment rate of $1.5\,\mathrm{km}^{-1}$ (solid red, solid blue, and dashed green) and $0.55\,\mathrm{km}^{-1}$ (dashed blue). Shell entrainment and detrainment rates, as well as core detrainment, are set equal to the core entrainment except for the case with a dashed green line, which uses a higher core detrainment of $1.7\,\mathrm{km}^{-1}$. The saturation moist static energy is shown with the thin black dotted line.

and Böing et al. (2012) have discussed theoretical arguments based on buoyancy-sorting ideas that suggest the opposite relationship between entrainment and humidity. Böing et al. (2012) also presented model results with varying environmental humidity that suggest detrainment exhibits a strong dependence on humidity, whereas entrainment exhibits a much weaker relationship. The approach used here can also be utilized to further explore the sensitivity of entrainment or dilution on various other factors, such as shear or stability, to help illuminate how entrainment and dilution can be more faithfully parameterized. Preliminary work on this suggests that the fractional entrainment increases modestly with increasing humidity consistent with Böing et al. (2012) and will be discussed in future work.

Mapes and Neale (2011) presented a convective parameterization that attempts to reproduce the effects of convective organization by allowing previous convection to reduce the entrainment rate of subsequent convection. The scheme also increases the probability of cloud overlap when convection becomes more organized. The importance of organized convection to various atmospheric phenomena, such as tropical waves, is still being explored. Nevertheless, the dilution metrics here could be beneficial for investigating the validity of similar approaches for implicit representations of organized convection.

Visual inspection of the bubble simulations reveals a tendency for the thermals to evolve toward a spherical geometry similar to the natural geometry of a Hill vortex

(Hill 1894), but they tend to stay slightly elongated as described by Hernandez-Deckers and Sherwood (2016). This may have important implications for the relationship between entrainment or dilution and radius, as well as the pattern of nonhydrostatic pressure perturbations that provide drag (Romps and Charn 2015). The degree of turbulence in these simulations makes attempts to quantify the aspect ratio of the thermals nearly impossible, but the results in Fig. 8 may change if the data could be categorized by geometric characteristics. Analyzing the evolution of more idealized buoyancy perturbations may provide further insight into how cloud geometry affects entrainment.

In addition to the need for a better understanding of what constrains entrainment and detrainment rates, the results here suggest that cloud heterogeneity is an important factor determining the amount of dilution for a given amount of entrainment, consistent with previous studies. In a way, we can interpret the low values of entrainment used by bulk plume models as a simple way to implicitly include the effects of cloud heterogeneity, which broadly achieves a similar rate of dilution (Fig. 22b). Sherwood et al. (2013) presented a less implicit method for treating cloud heterogeneity with some success. More explicit treatments of cloud heterogeneity like the buffered Lagrangian thermal model (Fig. 21) may help reproduce the observed moisture sensitivity of convection while using realistically large entrainment and without resorting to ad hoc parameters, which could potentially help rectify the issues surrounding the treatment of entrainment.

APPENDIX

Toy Lagrangian Thermal Model

a. Basic thermal without a shell

The three continuity equations for mass, vertical momentum, and a general thermodynamic tracer ϕ are

$$\frac{\partial \rho}{\partial t} + \nabla \cdot (\rho \mathbf{u}) = 0, \tag{A1}$$

$$\frac{\partial \rho w}{\partial t} + \nabla \cdot (\rho \mathbf{u} w) = -g\rho - \frac{dp}{dz}, \tag{A2}$$

$$\frac{\partial \rho \phi}{\partial t} + \nabla \cdot (\rho \mathbf{u} \phi) = S_\phi. \tag{A3}$$

Let us assume that ϕ is conserved ($S_\phi = 0$). It is useful to rewrite (A2) by subtracting a hydrostatic base state ($d\overline{p}/dz = -\overline{\rho}g$) to obtain

$$\frac{\partial \rho w}{\partial t} + \nabla \cdot (\rho \mathbf{u} w) = \overline{\rho} b - \frac{dp'}{dz}, \tag{A4}$$

where $b = -g\rho'/\overline{\rho}$ is buoyancy.

To describe the mass budget of a Lagrangian thermal, we will integrate (A1) over the predefined spherical volume of the thermal:

$$\iiint_V \frac{\partial \rho}{\partial t} d^3\mathbf{x} = -\iiint_V \nabla \cdot (\rho \mathbf{u}) d^3\mathbf{x}$$
$$= \iint_{\partial V} \hat{n} \cdot (\rho \mathbf{u}) d^2\mathbf{x}. \tag{A5}$$

On the left-hand side, the integral over density over a volume gives the total mass tendency over the volume. The right-hand side can be written as the surface integral of mass fluxes across the boundary of the thermal volume ∂V according to Gauss's theorem. This mass flux across the boundary of the volume corresponds to the net mass change due to entrainment and detrainment (de Rooy and Siebesma 2010). Thus, we can rewrite (A5) in a simpler form:

$$\frac{dm_c}{dt} = e - d, \tag{A6}$$

where m_c is the total mass of the thermal and e and d are the total mass entrainment and detrainment rates, respectively (kg s^{-1}). Entrainment and detrainment are usually represented as fractional values, so additionally, (A6) can be normalized by m_c to give fractional entrainment and detrainment time scales, ε_t and δ_t (s^{-1}):

$$\frac{dm_c}{dt} = m_c(\varepsilon_t - \delta_t). \tag{A7}$$

Performing a similar integration and normalization of (A3) yields a prognostic equation for the average ϕ of the thermal:

$$\frac{dm_c \phi_c}{dt} = m_c(\varepsilon_t \phi_e - \delta_t \phi_d), \tag{A8}$$

where ϕ_e and ϕ_d are the values of ϕ in the entraining and detraining air. Choosing ϕ to be a tracer such as moist static energy allows other thermodynamic variables to be diagnosed.

Similarly, we can integrate (A4) and neglect entrainment and detrainment of momentum (Dawe and Austin 2011b) to get

$$\frac{dm_c w_c}{dt} = m_c(B - D), \tag{A9}$$

where B and D represent the net accelerations due to buoyancy and drag. By using the ideal gas law and a virtual temperature correction, $T_v = T(1 + 0.61q_v)$, the net buoyancy acceleration can be written as

$$B = g\frac{T_v - \overline{T_v}}{\overline{T_v}}. \tag{A10}$$

Instead of estimating the pressure field around the thermal, the drag force can be estimated using a

simple form drag on a spherical volume (Romps and Charn 2015),

$$D = \frac{c_d A_c w_c^2}{2V_c}, \tag{A11}$$

where c_d is the drag coefficient and A_c and V_c are the cross-sectional area and volume of the thermal, respectively. Note that a spherical thermal is assumed in order to obtain the diagnosed area and volume from the mass.

b. Adding a cloud shell

To implement an explicit cloud shell, we will repeat the derivation of (A7) and (A8), considering two separate volumes that exchange mass according to Fig. 21 and normalizing by the thermal core mass. The shell component is only meant to be a thermodynamic buffer and, therefore, is dynamically passive in the sense that we will not consider its momentum. The new equations are as follows:

$$\frac{dm_c}{dt} = m_c(\varepsilon_c - \delta_c), \tag{A12}$$

$$\frac{dm_s}{dt} = m_c[\varepsilon_s - \delta_s - (\varepsilon_c - \delta_c)], \tag{A13}$$

$$\frac{dm_c\phi_c}{dt} = m_c(\varepsilon_c\phi_s - \delta_c\phi_c), \tag{A14}$$

$$\frac{dm_s\phi_s}{dt} = m_c[\varepsilon_s\overline{\phi} - \delta_s\phi_s - (\varepsilon_c\phi_s - \delta_c\phi_c)], \tag{A15}$$

where subscripts c and s indicate the thermal core and shell, respectively, and the overbar in (A15) indicates a horizontal average in the cloud-free environment.

REFERENCES

Arakawa, A., and W. H. Schubert, 1974: Interaction of a cumulus cloud ensemble with the large-scale environment, part I. *J. Atmos. Sci.*, **31**, 674–701, doi:10.1175/1520-0469(1974)031<0674:IOACCE>2.0.CO;2.

Bechtold, P., M. Köhler, T. Jung, F. Boblas-Reyes, M. Leutbecher, M. J. Rodwell, F. Vitart, and G. Balsamo, 2008: Advances in simulating atmospheric variability with the ECMWF model: From synoptic to decadal timescales. *Quart. J. Roy. Meteor. Soc.*, **134**, 1337–1351, doi:10.1002/qj.289.

Böing, S. J., A. P. Siebesma, J. D. Korpershoek, and H. J. J. Jonker, 2012: Detrainment in deep convection. *Geophys. Res. Lett.*, **39**, L20816, doi:10.1029/2012GL053735.

Bryan, G. H., J. C. Wyngaard, and J. M. Fritsch, 2003: Resolution requirements for the simulation of deep moist convection. *Mon. Wea. Rev.*, **131**, 2394–2416, doi:10.1175/1520-0493(2003)131<2394:RRFTSO>2.0.CO;2.

Chepfer, H., S. Bony, D. Winker, M. Chiriaco, J.-L. Dufresne, and G. Sèze, 2008: Use of CALIPSO lidar observations to evaluate the cloudiness simulated by a climate model. *Geophys. Res. Lett.*, **35**, L15704, doi:10.1029/2008GL034207.

Chikira, M., 2010: A cumulus parameterization with state-dependent entrainment rate. Part II: Impact on climatology in a general circulation model. *J. Atmos. Sci.*, **67**, 2194–2211, doi:10.1175/2010JAS3317.1.

——, and M. Sugiyama, 2010: A cumulus parameterization with state-dependent entrainment rate. Part I: Description and sensitivity to temperature and humidity profiles. *J. Atmos. Sci.*, **67**, 2171–2193, doi:10.1175/2010JAS3316.1.

Damiani, R., G. Vali, and S. Haimov, 2006: The structure of thermals in cumulus from airborne dual-Doppler radar observations. *J. Atmos. Sci.*, **63**, 1432–1450, doi:10.1175/JAS3701.1.

Dawe, J. T., and P. H. Austin, 2011a: Interpolation of LES cloud surfaces for use in direct calculations of entrainment and detrainment. *Mon. Wea. Rev.*, **139**, 444–456, doi:10.1175/2010MWR3473.1.

——, and ——, 2011b: The influence of the cloud shell on tracer budget measurements of LES cloud entrainment. *J. Atmos. Sci.*, **68**, 2909–2920, doi:10.1175/2011JAS3658.1.

——, and ——, 2013: Direct entrainment and detrainment rate distributions of individual shallow cumulus clouds in an LES. *Atmos. Chem. Phys.*, **13**, 7795–7811, doi:10.5194/acp-13-7795-2013.

Deardorff, J. W., 1980: Cloud top entrainment instability. *J. Atmos. Sci.*, **37**, 131–147, doi:10.1175/1520-0469(1980)037<0131:CTEI>2.0.CO;2.

Dee, D., and Coauthors, 2011: The ERA-Interim reanalysis: Configuration and performance of the data assimilation system. *Quart. J. Roy. Meteor. Soc.*, **137**, 553–597, doi:10.1002/qj.828.

Del Genio, A. D., 2012: Representing the sensitivity of convective cloud systems to tropospheric humidity in general circulation models. *Surv. Geophys.*, **33**, 637–656, doi:10.1007/s10712-011-9148-9.

Derbyshire, S. H., I. Beau, P. Bechtold, J.-Y. Grandpeix, J.-M. Pirou, J.-L. Redelsperger, and P. M. M. Soares, 2004: Sensitivity of moist convection to environmental humidity. *Quart. J. Roy. Meteor. Soc.*, **130**, 3055–3079, doi:10.1256/qj.03.130.

de Rooy, W. C., and A. P. Siebesma, 2008: A simple parameterization for detrainment in shallow cumulus. *Mon. Wea. Rev.*, **136**, 560–576, doi:10.1175/2007MWR2201.1.

——, and ——, 2010: Analytical expressions for entrainment and detrainment in cumulus convection. *Quart. J. Roy. Meteor. Soc.*, **136**, 1216–1227, doi:10.1002/qj.640.

——, and Coauthors, 2013: Entrainment and detrainment in cumulus convection: An overview. *Quart. J. Roy. Meteor. Soc.*, **139**, 1–19, doi:10.1002/qj.1959.

Emanuel, K. A., 1994: *Atmospheric Convection.* Oxford University Press, 588 pp.

Grabowski, W. W., and T. L. Clark, 1993: Cloud-environment interface instability. Part II: Extension to three spatial dimensions. *J. Atmos. Sci.*, **50**, 555–573, doi:10.1175/1520-0469(1993)050<0555:CEIIPI>2.0.CO;2.

Grant, A. L. M., and A. R. Brown, 1999: Similarity hypothesis for shallow-cumulus transports. *Quart. J. Roy. Meteor. Soc.*, **125**, 1913–1936, doi:10.1002/qj.49712555802.

Hannah, W. M., and E. D. Maloney, 2011: The role of moisture–convection feedbacks in simulating the Madden–Julian oscillation. *J. Climate*, **24**, 2754–2770, doi:10.1175/2011JCLI3803.1.

——, and ——, 2014: The moist static energy budget in NCAR CAM5 hindcasts during DYNAMO. *J. Adv. Model. Earth Syst.*, **6**, 420–440, doi:10.1002/2013MS000272.

Hernandez-Deckers, D., and S. C. Sherwood, 2016: A numerical investigation of cumulus thermals. *J. Atmos. Sci.*, **73**, 4117–4136, doi:10.1175/JAS-D-15-0385.1.

Heus, T., and H. J. J. Jonker, 2008: Subsiding shells around shallow cumulus clouds. *J. Atmos. Sci.*, **65**, 1003–1018, doi:10.1175/2007JAS2322.1.

Hill, M. J. M., 1894: On a spherical vortex. *Philos. Trans. Roy. Soc. London*, **185A**, 213–245, doi:10.1098/rsta.1894.0006.

Igel, M. R., and S. C. van den Heever, 2015: Tropical, oceanic, deep convective cloud morphology as observed by CloudSat. *Atmos. Chem. Phys. Discuss.*, **15**, 15 977–16 017, doi:10.5194/acpd-15-15977-2015.

Johari, H., 1992: Mixing in thermals with and without buoyancy reversal. *J. Atmos. Sci.*, **49**, 1412–1426, doi:10.1175/1520-0469(1992)049<1412:MITWAW>2.0.CO;2.

Jonas, P. R., 1990: Observations of cumulus cloud entrainment. *Atmos. Res.*, **25**, 105–127, doi:10.1016/0169-8095(90)90008-Z.

Jorgensen, D. P., and M. A. LeMone, 1989: Vertical velocity characteristics of oceanic convection. *J. Atmos. Sci.*, **46**, 621–640, doi:10.1175/1520-0469(1989)046<0621:VVCOOC>2.0.CO;2.

Kain, J. S., and J. M. Fritsch, 1990: A one-dimensional entraining/detraining plume model and its application in convective parameterization. *J. Atmos. Sci.*, **47**, 2784–2802, doi:10.1175/1520-0469(1990)047<2784:AODEPM>2.0.CO;2.

Khairoutdinov, M. F., and D. A. Randall, 2003: Cloud resolving modeling of the ARM summer 1997 IOP: Model formulation, results, uncertainties, and sensitivities. *J. Atmos. Sci.*, **60**, 607–625, doi:10.1175/1520-0469(2003)060<0607:CRMOTA>2.0.CO;2.

——, and ——, 2006: High-resolution simulation of shallow-to-deep convection transition over land. *J. Atmos. Sci.*, **63**, 3421–3436, doi:10.1175/JAS3810.1.

Kim, D., A. H. Sobel, E. D. Maloney, D. M. W. Frierson, and I.- S. S. Kang, 2011: A systematic relationship between intraseasonal variability and mean state bias in AGCM simulations. *J. Climate*, **24**, 5506–5520, doi:10.1175/2011JCLI4177.1.

Klaassen, G. P., and T. L. Clark, 1985: Dynamics of the cloud–environment interface and entrainment in small cumuli: Two-dimensional simulations in the absence of ambient shear. *J. Atmos. Sci.*, **42**, 2621–2642, doi:10.1175/1520-0469(1985)042<2621:DOTCEI>2.0.CO;2.

Kuethe, A. M., 1935: Investigations of the turbulent mixing regions formed by jets. *J. Appl. Mech.*, **2**, 87–95.

Langhans, W., K. Yeo, and D. M. Romps, 2015: Lagrangian investigation of the precipitation efficiency of convective clouds. *J. Atmos. Sci.*, **72**, 1045–1062, doi:10.1175/JAS-D-14-0159.1.

LeMone, M. A., and E. J. Zipser, 1980: Cumulonimbus vertical velocity events in GATE. Part I: Diameter, intensity and mass flux. *J. Atmos. Sci.*, **37**, 2444–2457, doi:10.1175/1520-0469(1980)037<2444:CVVEIG>2.0.CO;2.

Levine, J., 1959: Spherical vortex theory of bubble-like motion in cumulus clouds. *J. Meteor.*, **16**, 653–662, doi:10.1175/1520-0469(1959)016<0653:SVTOBL>2.0.CO;2.

Lu, C., Y. Liu, S. S. Yum, S. Niu, and S. Endo, 2012: A new approach for estimating entrainment rate in cumulus clouds. *Geophys. Res. Lett.*, **39**, L04802, doi:10.1029/2011GL050546.

Lucas, C., E. J. Zipser, and M. A. Lemone, 1994: Vertical velocity in oceanic convection off tropical Australia. *J. Atmos. Sci.*, **51**, 3183–3193, doi:10.1175/1520-0469(1994)051<3183:VVIOCO>2.0.CO;2.

Luo, Z., J. Jeyaratnam, S. Iwasaki, H. Takahashi, and R. Anderson, 2014: Convective vertical velocity and cloud internal vertical structure: An A-Train perspective. *Geophys. Res. Lett.*, **41**, 723–729, doi:10.1002/2013GL058922.

Maloney, E. D., and D. Hartmann, 2001: The sensitivity of intraseasonal variability in the NCAR CCM3 to changes in convective parameterization. *J. Climate*, **14**, 2015–2034, doi:10.1175/1520-0442(2001)014<2015:TSOIVI>2.0.CO;2.

Mapes, B. E., and R. Neale, 2011: Parameterizing convective organization to escape the entrainment dilemma. *J. Adv. Model. Earth Syst.*, **3**, M06004, doi:10.1029/2011MS000042.

McCarthy, J., 1974: Field verification of the relationship between entrainment rate and cumulus cloud diameter. *J. Atmos. Sci.*, **31**, 1028–1039, doi:10.1175/1520-0469(1974)031<1028:FVOTRB>2.0.CO;2.

Moorthi, S., and M. Suarez, 1992: Relaxed Arakawa–Schubert: A parameterization of moist convection for general circulation models. *Mon. Wea. Rev.*, **120**, 978–1002, doi:10.1175/1520-0493(1992)120<0978:RASAPO>2.0.CO;2.

Morton, B. R., G. Taylor, and J. S. Turner, 1956: Turbulent gravitational convection from maintained and instantaneous sources. *Proc. Roy. Soc. London*, **234A**, 1–23, doi:10.1098/rspa.1956.0011.

Neggers, R., A. P. Siebesma, and H. J. J. Jonker, 2002: A multiparcel model for shallow cumulus convection. *J. Atmos. Sci.*, **59**, 1655–1668, doi:10.1175/1520-0469(2002)059<1655:AMMFSC>2.0.CO;2.

Rickenbach, T. M., and S. A. Rutledge, 1998: Convection in TOGA COARE: Horizontal scale, morphology, and rainfall production. *J. Atmos. Sci.*, **55**, 2715–2729, doi:10.1175/1520-0469(1998)055<2715:CITCHS>2.0.CO;2.

Romps, D. M., 2010: A direct measure of entrainment. *J. Atmos. Sci.*, **67**, 1908–1927, doi:10.1175/2010JAS3371.1.

——, and Z. Kuang, 2010: Do undiluted convective plumes exist in the upper tropical troposphere? *J. Atmos. Sci.*, **67**, 468–484, doi:10.1175/2009JAS3184.1.

——, and A. B. Charn, 2015: Sticky thermals: Evidence for a dominant balance between buoyancy and drag in cloud updrafts. *J. Atmos. Sci.*, **72**, 2890–2901, doi:10.1175/JAS-D-15-0042.1.

Salzen, K. V., and N. McFarlane, 2002: Parameterization of the bulk effects of lateral and cloud-top entrainment in transient shallow cumulus clouds. *J. Atmos. Sci.*, **59**, 1405–1430, doi:10.1175/1520-0469(2002)059<1405:POTBEO>2.0.CO;2.

Saunders, P. M., 1962: Penetrative convection in stably stratified fluids. *Tellus*, **2**, 177–194, doi:10.1111/j.2153-3490.1962.tb00130.x.

Schumacher, C., S. N. Stevenson, and C. R. Williams, 2015: Vertical motions of the tropical convective cloud spectrum over Darwin, Australia. *Quart. J. Roy. Meteor. Soc.*, **141**, 2277–2288, doi:10.1002/qj.2520.

Scorer, R. S., 1957: Experiments on convection of isolated masses of buoyant fluid. *J. Fluid Mech.*, **2**, 583–594, doi:10.1017/S0022112057000397.

Sherwood, S. C., D. Hernández-Deckers, M. Colin, and F. Robinson, 2013: Slippery thermals and the cumulus entrainment paradox. *J. Atmos. Sci.*, **70**, 2426–2442, doi:10.1175/JAS-D-12-0220.1.

Siebesma, A., and J. Cuijpers, 1995: Evaluation of parametric assumptions for shallow cumulus convection. *J. Atmos. Sci.*, **52**, 650–666, doi:10.1175/1520-0469(1995)052<0650:EOPAFS>2.0.CO;2 .

Simpson, J., 1971: On cumulus entrainment and one-dimensional models. *J. Atmos. Sci.*, **28**, 449–455, doi:10.1175/1520-0469(1971)028<0449:OCEAOD>2.0.CO;2.

Sloss, P., 1967: An empirical examination of cumulus entrainment. *J. Appl. Meteor.*, **6**, 878–881, doi:10.1175/1520-0450(1967)006<0878:AEEOCE>2.0.CO;2.

Stirling, J., and R. A. Stratton, 2012: Entrainment processes in the diurnal cycle of deep convection over land. *Quart. J. Roy. Meteor. Soc.*, **138**, 1135–1149, doi:10.1002/qj.1868.

Stith, J. L., 1992: Observations of cloud-top entrainment in cumuli. *J. Atmos. Sci.*, **49**, 1334–1347, doi:10.1175/1520-0469(1992)049<1334:OOCTEI>2.0.CO;2.

Tiedtke, M., 1989: A comprehensive mass flux scheme for cumulus parameterization. *Mon. Wea. Rev.*, **117**, 1779–1800, doi:10.1175/1520-0493(1989)117<1779:ACMFSF>2.0.CO;2.

Tokioka, T., K. Yamazaki, A. Kitoh, and T. Ose, 1988: The equatorial 30-60 day oscillation and the Arakawa-Schubert penetrative cumulus parameterization. *J. Meteor. Soc. Japan*, **66**, 883–901, doi:10.2151/jmsj1965.66.6_883.

Turner, J. S., 1963: The motion of buoyant elements in turbulent surroundings. *J. Fluid Mech.*, **16**, 1–16, doi:10.1017/S0022112063000549.

Uma, K. N., and T. N. Rao, 2009: Characteristics of vertical velocity cores in different convective systems observed over Gadanki, India. *Mon. Wea. Rev.*, **137**, 954–975, doi:10.1175/2008MWR2677.1.

Varble, A., and Coauthors, 2014: Evaluation of cloud-resolving and limited area model intercomparison simulations using TWP-ICE observations: 1. Deep convective updraft properties. *J. Geophys. Res. Atmos.*, **119**, 13 891–13 918, doi:10.1002/2013JD021371.

Wagner, T. M., and H.-F. Graf, 2010: An ensemble cumulus convection parameterization with explicit cloud treatment. *J. Atmos. Sci.*, **67**, 3854–3869, doi:10.1175/2010JAS3485.1.

Williams, E. R., S. A. Rutledge, S. G. Geotis, N. Renno, E. Rasmussen, and T. Rikenbach, 1992: A radar and electrical study of tropical ''hot towers.'' *J. Atmos. Sci.*, **49**, 1386–1395, doi:10.1175/1520-0469(1992)049<1386:ARAESO>2.0.CO;2.

Woodward, B., 1959: The motion in and around isolated thermals. *Quart. J. Roy. Meteor. Soc.*, **85**, 144–151, doi:10.1002/qj.49708536407.

Yeo, K., and D. M. Romps, 2013: Measurement of convective entrainment using Lagrangian particles. *J. Atmos. Sci.*, **70**, 266–277, doi:10.1175/JAS-D-12-0144.1.

Zhang, G. J., and N. A. McFarlane, 1995: Sensitivity of climate simulations to the parameterization of cumulus convection in the Canadian climate centre general circulation model. *Atmos.–Ocean*, **33**, 407–446, doi:10.1080/07055900.1995.9649539.

Zhang, Y., S. A. Klein, J. Boyle, and G. G. Mace, 2010: Evaluation of tropical cloud and precipitation statistics of Community Atmosphere Model version 3 using CloudSat and CALIPSO data. *J. Geophys. Res.*, **115**, D12205, doi:10.1029/2009JD012006.

Zhao, M., and P. Austin, 2005: Life cycle of numerically simulated shallow cumulus clouds. Part II: Mixing dynamics. *J. Atmos. Sci.*, **62**, 1291–1310, doi:10.1175/JAS3415.1.